Cite: Zhiming Gao, Josh Pihl, Tim LaClair, Brian Fricke. (2021) Global Kinetic Modeling of NH_3-SCR with Two Sites of NH_3 Storage on Cu-SSZ-13. Chemical Engineering Journal, Vol. 406, 127120. https://doi.org/10.1016/j.cej.2020.127120

Global Kinetic Modeling of NH_3-SCR with Two Sites of NH_3 Storage on Cu-SSZ-13

Zhiming Gao, Josh Pihl, Tim LaClair, Brian Fricke

Oak Ridge National Laboratory
P.O. Box 2008
Oak Ridge, TN 37831

Corresponding author: Zhiming Gao
Email address: gaoz@ornl.gov
Tel: +1-865-341-1339
Oak Ridge National Laboratory
Oak Ridge, TN 37831

Cite: Zhiming Gao, Josh Pihl, Tim LaClair, Brian Fricke. (2021) Global Kinetic Modeling of NH_3-SCR with Two Sites of NH_3 Storage on Cu-SSZ-13. Chemical Engineering Journal, Vol. 406, 127120. https://doi.org/10.1016/j.cej.2020.127120

Abstract

A comprehensive selective catalytic reduction (SCR) model is developed to detail the global kinetic reactions in the catalyst which is involved in two type of sites for high- and low-temperature NH_3 adsorption/desorption, as well as a low temperature H_2O storage. The model accounts for the formation of ammonium nitrate in fast SCR and the decomposition formation of ammonium nitrate in the absence of NO, and addresses N_2O relative to NO and NO_2 reactions with NH_3. The model has been validated against commercial Cu-SSZ-13 measurements of NH_3 inventory, NH_3 oxidation, NO oxidation, standard SCR, fast SCR and NO_2 SCR at both comprehensive steady-state and transient conditions. In addition, the application of the SCR model for emissions control over a transient drive cycle at cold start was demonstrated based on diesel oxidation catalyst (DOC) and SCR aftertreatment system for a passenger car. The results show that the SCR model can provide the detailed emissions estimations for steady-state and transient conditions, can assist with understanding the impact of the SCR reaction mechanism, and can assist with the design and optimization of SCR catalysts to develop innovative technologies for co-optimization of engine fuel economy and emissions control technologies.

Key Words: SCR Kinetic Modeling, Two-site NH_3 storage, Ammonium Nitrate, Transient, Drive cycle Emissions

Highlights:

- Global kinetic SCR model for NH_3 inventory, NH_3 oxidation, NO oxidation, SCRs and N_2O formation
- NH_3 inventory mechanism with two-sites of NH3 storage and one site of H_2O storage
- Ammonium nitrate formation included in fast SCR and its decomposition in the absence of NO
- SCR model numerical application for steady-state and transient drive cycle emissions control

Graphical Abstract

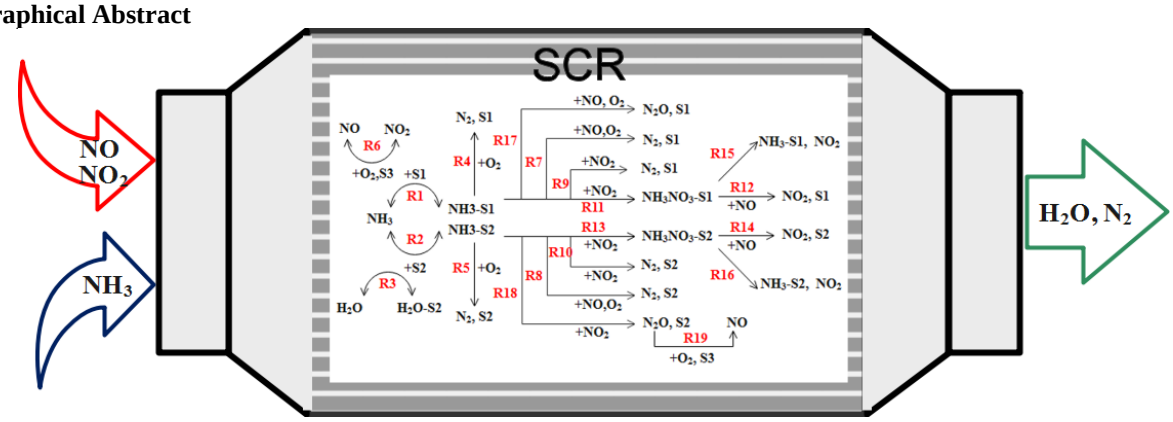

Cite: Zhiming Gao, Josh Pihl, Tim LaClair, Brian Fricke. (2021) Global Kinetic Modeling of NH_3-SCR with Two Sites of NH_3 Storage on Cu-SSZ-13. Chemical Engineering Journal, Vol. 406, 127120. https://doi.org/10.1016/j.cej.2020.127120

1. Introduction

Advanced lean combustion engines enable significantly higher thermal efficiency than stoichiometric combustion engines, but also bring a substantial challenge for NOx emissions control. Two prominent lean NOx emissions control technologies are lean NOx traps (LNTs) and selective catalytic reduction (SCR). Considering the durability, reliability and cost-effectiveness [1], the SCR technology is generally considered more attractive for removing NOx from lean exhausts in automobile applications.

SCR catalysts have evolved since their introduction into automobile applications about 16 years ago [2]. The first-generation of SCRs use vanadia (vanadium(V) oxide, V_2O_5) supported on titania (titanium dioxide, TiO_2), which were widely used in aftertreatment systems for stationary power systems [2-4]. Compared to vanadia-based catalysts, zeolite-based SCR catalysts exhibit significantly higher NOx conversion efficiency over a wider range of temperatures. Zeolite-based SCRs, particularly copper- and iron-exchanged zeolites (Cu-zeolites [5-7] and Fe-zeolites [8-10], respectively), have been identified as a primary pathway for the refinement and enhancement of SCR technologies for lean NOx emission control in vehicle applications. Cu-zeolites achieve improved low-temperature performance with larger ammonia storage and higher NOx reduction efficiency, while Fe-zeolites typically function better at high temperature [11]. The zeolites used in SCRs are evolved from large-pore 12-membrane ring type zeolites (e.g., beta or BEA) and medium-pore 10-membrane ring type zeolites (e.g. ZSM-5 or MFI) to the contemporary small-pore eight-membrane ring type zeolites (e.g., chabazite or CHA). The chabazite structures demonstrate promising properties due to their high thermal stability even when exposed to extreme aging conditions [12], but also show decent hydrocarbon resistance due to the small size of the openings in the 0.38 nm-diameter structure (i.e., most hydrocarbons cannot access the CHA pores, minimizing the effect of hydrocarbon poisoning [12-13]). At present, two CHA-type zeolite-based SCRs, including Cu-SSZ-13 and Cu-SAPO-34, are commercialized as lean NOx after-treatment catalysts [14]. Compared to Cu-SSZ-13, Cu-SAPO-34 shows improved NOx conversion and N_2O selectivity, but its low-temperature performance is degraded in the presence of water [15-16]. Thus, the relatively simple structure of Cu-SSZ-13 is becoming more attractive in vehicle applications, and it is widely used to understand in-depth SCR chemistry and reaction mechanisms.

A great number of kinetic models have been developed for various SCR catalysts [8-10, 17-33], including vanadium-based SCR [17-19], Fe-zeolites [8-10,20-21], HZSM-5 [22-23], Cu-BEA [14, 29], Cu-ZSM-5 [24-25], Cu-CHA [21, 26-28, 30] and many others [31-33]. Most of these kinetic models account for the basic features of NH_3 adsorption/desorption, NH_3 oxidation, NO oxidation and three basic selective catalytic reductions (i.e. NO-SCR, Fast-SCR and NO_2-SCR). For example, Supriyanto et.al. [14], Olsson et.al. [24], Gao et.al. [25], Song et.al. [27] and Shibata et.al. [34], adopted the simple global kinetic mechanism of NH_3 adsorption/desorption with a single storage site for modeling the SCR catalyst. These kinetic models do not address intermediate species that form within SCR NH_3-NO-NO_2/O_2 reacting system. In fact, the reactions for the reduction of NO only, $NO+NO_2$ and NO_2 can be divided into several steps involved in intermediate species, like nitrite and nitrate. Sjövall et.al. [20] and Daya et.al. [2] introduced ammonium nitrate formation from NO_2 and NH_3 in their models and added ammonium nitrate decomposition to NO_2 or N_2O. Singh and Bhatia [35] also presented a simple kinetic model including nitrate, but the mechanism of nitrate in fast SCR was ignored. The experiments of Ciardelli et.al. [36] and Nova et.al. [37] indicate that SCR NH_3-NO-NO_2/O_2 reactions are involved in (1) NO_2 is converted to nitrous and nitric acid via NO_2 disproportion, dimerization and reaction with water; (2) nitrous acid in the presence of NH_3 forms unstable ammonium nitrite which readily decomposes to N_2 and water; (3) nitric acid reacts with NH_3 to form more stable ammonium nitrate; and (4) in the absence of a reducing agent, ammonium nitrate may behave as a terminal product or may be thermally decomposed to NO_2 (or maybe N_2O) at higher temperature. Similar observations were also reported by others [38, 39]. Including these reaction mechanisms in the kinetic models is necessary to properly predict the experimental observations. However, the current SCR models are unable to provide comprehensive kinetic models to account for the experimental observations noted above. In particular, the current SCR models remain inadequate to account for the observation that NO_2 is responsible for the formation of NH_4NO_3, and NH_4NO_3 no longer behaves as a terminal product and actively reacts with NO to form N_2 in the presence of NO [37]. Furthermore, the experimental results show that the reaction rate between NH_4NO_3 and NO is essentially equal to that of the fast SCR reaction. It remains unclear how to treat rapidly-formed intermediate products (i.e. HNO_2, HNO3, and ammonium nitrite) in the SCR kinetic modeling. Another important reaction which should be considered in SCR kinetic models is N_2O formation, which should have multiple pathways to generate N_2O from NO and NO_2 reactions with NH_3. However, the current kinetic mechanisms available do not address these critical issues clearly.

Moreover, most SCR kinetic models in the public domain are based on a single type of storage site for NH_3 adsorption/desorption. However, the latest small-pore zeolites are known to function with multiple types of storage sites [2, 20, 26-27, 40]. For the example of Cu-SSZ-13, depending on the method of synthesis, the storage and reactivity sites are typically Cu active sites and Brönsted acid sites located within the zeolite structure [41]. Experimental observations show ammonia desorption at both high and low temperature [20, 40]. NH_3 storage at low temperatures (i.e. < 200 °C) is typically captured by a physisorbed site and additional low-temperature adsorption on copper sites and Brønsted acid sites [42]. Due to the complexity of storage site identification, multiple types of storage sites were investigated recently [2, 26, 43], but existing models do not comprehensively address multiple storage sites together with intermediate species occurring in SCR NH_3-NO-NO_2/O_2 reacting systems. In addition, for vehicle applications, SCR takes place in the presence of

Cite: Zhiming Gao, Josh Pihl, Tim LaClair, Brian Fricke. (2021) Global Kinetic Modeling of NH_3-SCR with Two Sites of NH_3 Storage on Cu-SSZ-13. Chemical Engineering Journal, Vol. 406, 127120. https://doi.org/10.1016/j.cej.2020.127120

complex exhaust flows that include significant water content, which may affect NH_3 adsorption in zeolite-based SCRs. However, there are still very few kinetic models that enable H_2O adsorption and desorption in real mobile emissions control [44, 45].

Therefore, in this paper, a comprehensive model is developed to account for the global kinetic reactions between NH_3 and NOx interacting with the SCR catalyst, including two types of sites for NH_3 storage, as well as a H_2O storage. The model considers SCR reactions at both sites. Moreover, the model includes the formation and decomposition of ammonium nitrate, and addresses N_2O relative to NO and NO_2 reactions with NH_3. The model has been compared with comprehensive experimental data measured at the Oak Ridge National Laboratory (ORNL) based on a series of SCR reactor experimental protocols. The SCR model application for emissions control over a transient drive cycle is also explored and demonstrated. The following sections describe the SCR modeling approach and compare simulation results with experimental data.

2. NH_3 SCR Modeling Approach

2.1. SCR flow modeling

The SCR flow model was developed along the same lines as our after-treatment models published previously [46-47]. The SCR device is considered in the model as parallel one-dimensional channels of a catalytic monolith, through which exhaust gas flows in a fully developed laminar flow. All species reactions are assumed to occur in the solid phase interface on the SCR washcoat. To account for the effect of temperature changes on catalyst activity, a transient energy balance, as well as a species mass balance, is included. Temperatures and concentrations are assumed to vary only in the axial direction.
The governing equation for the gas-phase energy is given as

$$\rho_g c_{pg} \varepsilon \left(\frac{\partial T_g}{\partial t} + u_g \frac{\partial T_g}{\partial z} \right) = h_g G_m \left(T_s - T_g \right) \tag{1}$$

The governing equation for gas-phase species transport is expressed as

$$\frac{\partial x_{g_i}}{\partial t} + u_g \frac{\partial x_{g_i}}{\partial z} = \frac{h_m G_m}{\varepsilon} \left(x_{s_i} - x_{g_i} \right) \tag{2}$$

The governing equation for the solid-phase energy can be described as

$$\rho_s c_{ps} (1-\varepsilon) \frac{\partial T_s}{\partial t} = k_s (1-\varepsilon) \frac{\partial^2 T_s}{\partial z^2} + h_g G_m \left(T_g - T_s \right) + h_a G_a \left(T_a - T_s \right) + \sum_{k=1}^{n} R^k \cdot \Delta H^k \tag{3}$$

The catalytic surface species equation is described as

$$\frac{\partial x_{s_i}}{\partial t} = \frac{h_m G_m}{\varepsilon' (1-\varepsilon)} \left(x_{g_i} - x_{s_i} \right) + \frac{1}{\rho_m \varepsilon' (1-\varepsilon)} \sum_k \alpha_i^k R^k \tag{4}$$

The exhaust flow is considered as a fully developed laminar flow; heat and mass transfer coefficients in the equations (1-4) are determined by correlations for the average Nusselt Number and Sherwood Number [46], as follows:

$$Nu = 3.657 \left(1 + 0.095 \cdot Re \cdot Pr \cdot \left(\frac{D_h}{z} \right) \right)^{0.45} \tag{5}$$

$$Sh = 4.364 \left(1 + 0.095 \cdot Re \cdot Sc \cdot \left(\frac{D_h}{z} \right) \right)^{0.45} \tag{6}$$

2.2. SCR reaction mechanism

The SCR model focuses on estimating the global reaction rate between the ammonia and nitrogen oxides reaching the SCR catalyst. The key steps include NH_3 adsorption and desorption on the catalyst and multiple reactions between the adsorbed NH_3 and NO and NO_2. The SCR material investigated is Cu-SSZ-13, a commercial SCR formulation. Existing literature indicates that a single site model

does not accurately describe the experimental behavior of the catalytic reaction [2, 26, 40]. In fact, it has been suggested that NH_3 storage, oxidation and SCR reactions occur on multiple types of copper species for Cu-SSZ-13. Therefore, two site types were used in the present model. The S1 sites, which are used to characterize high-temperature NH_3 storage, are mainly at Cu sites and Bronsted acid sites; while the S2 sites, which account for low-temperature loosely bound NH_3 storage activities, are physisorbed sites , as well as some copper sites and Brønsted acid sites for additional low temperature adsorption. Moreover, for NH_3 adsorption under low temperature conditions, the impact of H_2O competitive adsorption on NH_3 storage at S2 sites is included based on the experiments and kinetic mechanism reported in [45]. The H_2O competitive adsorption on NH_3 storage is a common characteristic of real SCR applications, but this has been commonly ignored in most current SCR models. NH_3 adsorption/desorption and H_2O adsorption/desorption are addressed in Eqs. 7-9:

R1: $NH_3 + S1^* \Leftrightarrow NH_3S1^*$ (7)

R2: $NH_3 + S2^* \Leftrightarrow NH_3S2^*$ (8)

R3: $H_2O + S2^* \Leftrightarrow H_2OS2^*$ (9)

To account for NH_3 oxidation by oxygen, two global reactions on both site S1 and site S2 are considered:

R4: $2NH_3S1^* + 1.5O_2 \Rightarrow N_2 + 3H_2O + 2S1^*$ (10)

R5: $2NH_3S2^* + 1.5O_2 \Rightarrow N_2 + 3H_2O + 2S2^*$ (11)

The NO oxidation is assumed to only occur at the copper site which is a 3rd site, S3 and is different from the NH_3 storage sites. This assumption is also recommended by Daya et al. [2].

R6: $NO + 0.5O_2 \Leftrightarrow NO_2$ (12)

Three SCR reactions take place at both NH_3 storage sites S1 and S2. The standard NH_3 SCR reactions are given by:

R7: $4NH_3S1^* + 4NO + O_2 \Rightarrow 4N_2 + 6H_2O + 4S1^*$ (13)

R8: $4NH_3S2^* + 4NO + O_2 \Rightarrow 4N_2 + 6H_2O + 4S2^*$ (14)

The NO_2 SCR reactions are given by:

R9: $4NH_3S1^* + 3NO_2 \Rightarrow 3.5N_2 + 6H_2O + 4S1^*$ (15)

R10: $4NH_3S2^* + 3NO_2 \Rightarrow 3.5N_2 + 6H_2O + 4S2^*$ (16)

Although the fast SCR reaction has been recognized since the 1980s, the complete details are still not fully understood. Several experimental observations [26, 36, 37] indicate that the reduction of NO and NO_2 by NH_3 involves the formation of HNO_2 and HNO_3, both of which react independently with NH_3, generating unstable NH_4NO_2 and more stable NH_4NO_3, respectively. NH_4NO_2 decomposes rapidly to N_2 and H_2O. NH_4NO_3 reacts with NO to form N_2 and NO_2, and the reaction rate is essentially equal to that of the fast SCR reaction [37]. Therefore, for the SCR reaction, HNO_2, HNO_3 and NH_4NO_2 are unstable intermediate products from the conversion of NH_3-NO-NO_2 to N_2 and H_2O; whereas the formation of NH_4NO_3 is more stable. Compared to NH_4NO_3 formation and other reactions in SCR catalyst, the residual time of HNO_2, HNO_3 and NH_4NO_2 is extremely short. Therefore, these unstable intermediate products are not considered in the model to avoid extra small time step required in the modeling. Instead, to understand the in-depth chemistry of fast SCR reactions and to determine the optimal equimolar NO to NO_2 feed rate, as well as the impact of NH_4NO_3, a sequential scheme is adopted [26, 37], whereby the fast SCR reaction results from the intermediate formation of NH_4NO_3 and its subsequent reduction by NO (see Table 1):

Table 1. Chemistry mechanism of the fast SCR reaction involved in intermediate formation of NH_4NO_3.

$2NH_3 + 2NO_2 \Rightarrow N_2 + NH_4NO_3 + H_2O$
$NH_4NO_3 + NO \Rightarrow NO_2 + N_2 + 2H_2O$

Cite: Zhiming Gao, Josh Pihl, Tim LaClair, Brian Fricke. (2021) Global Kinetic Modeling of NH_3-SCR with Two Sites of NH_3 Storage on Cu-SSZ-13. Chemical Engineering Journal, Vol. 406, 127120. https://doi.org/10.1016/j.cej.2020.127120

$$2NH_3 + NO + NO_2 \Rightarrow 2N_2 + 3H_2O$$

Therefore, the fast SCR reactions (see Table 1) at NH_3 storage sites S1 and S2 are shown in Eqs. 17-20 via the simplification of not considering unstable intermediate products. The mechanism accounts very well for the observations that NO_2 is responsible for the formation of NH_4NO_3, and NH_4NO_3 is eventually converted to N_2 in the presence of NO [37].

R11: $2NH_3S1^* + 2NO_2 \Rightarrow N_2 + NH_4NO_3S1^* + H_2O$ (17)

R12: $NH_4NO_3S1^* + NO \Rightarrow NO_2 + N_2 + 2H_2O + S1^*$ (18)

R13: $2NH_3S2^* + 2NO_2 \Rightarrow N_2 + NH_4NO_3S2^* + H_2O$ (19)

R14: $NH_4NO_3S2^* + NO \Rightarrow NO_2 + N_2 + 2H_2O + S2^*$ (20)

Considering the experimental observation that in the absence of NO, NH_4NO_3 either behaves as a terminal product at lower temperature, or decompose to NO_2 at high temperature [20, 26, 36], two global reactions were added to describe ammonium nitrate decomposition, again employing the simplification of not considering unstable intermediate products.

R15: $NH_4NO_3S1^* \Rightarrow NH_3S1^* + NO_2 + 0.25O_2 + 0.5H_2O$ (21)

R16: $NH_4NO_3S2^* \Rightarrow NH_3S2^* + NO_2 + 0.25O_2 + 0.5H_2O$ (22)

Another important reaction in SCR kinetic models is N_2O formation. NH_4NO_3 may decompose to N_2O and H_2O [2], but the main part of N_2O formation is contributed from the NH_3 reaction with NO_2 or NO [20]. Thus, two reactions for N_2O formation and dissociation are considered below. The reactions address multiple pathways to generate N_2O related to NO and NO_2 reactions with NH_3.

R17: $2NH_3S1^* + 2NO + O_2 \Rightarrow N_2 + N_2O + 3H_2O + 2S1^*$ (23)

R18: $2NH_3S2^* + 2NO_2 \Rightarrow N_2 + N_2O + 3H_2O + 2S2^*$ (24)

In addition, N_2O oxidation is also considered in the current SCR kinetic model.

R19: $N_2O + 0.5O_2 \Rightarrow 2NO$ (25)

Thus, the above model describes a comprehensive kinetic mechanism related to stable intermediate products. All the reaction rates for (R1)-(R19) are described using the Arrhenius equation $k = A\exp^{-E_A/RT}$ (as listed in Table 2). In Table 2, the parameters of the reaction rates related to NH_3 adsorption and desorption and H_2O adsorption and desorption are adopted from the literature [45]. These were fitted with experimental measurements of a commercial Cu-SSZ-13 SCR catalyst according to the CLEERS transient SCR characterization protocol [45]. These data were used to develop and validate the presented model.

Table 2. The constants of reaction rate employed in the SCR model.

Description	Reaction	Pre-exp factor, A (mol/mol-site-s)	Activation energy, E_A (J/mol)
NH_3 adsorption on S1	$R_{1,f} = A_{1,f} \cdot x_{NH_3} \cdot \left(1 - \theta_{NH_3-S1^*} - \theta_{NH_4NO_3-S1^*}\right) \cdot \Psi_{S1^*}$	30.25	-
NH_3 desorption on S1	$R_{1,b} = A_{1,b} \cdot \exp(-E_{1,b}/RT) \cdot \theta_{NH_3-S1^*} \cdot \Psi_{S1^*}$	30.25/1.8E-3*	75E3*
NH_3 adsorption on S2	$R_{2,f} = A_{2,f} \cdot x_{NH_3} \cdot \left(1 - \theta_{NH_3-S2^*} - \theta_{NH_4NO_3-S2^*} - \theta_{H_2O-S2^*}\right) \cdot \Psi_{S2^*}$	1.853e3	-
NH_3 desorption on S2	$R_{2,b} = A_{2,b} \cdot \exp(-E_{2,b}/RT) \cdot \theta_{NH_3-S2^*} \cdot \Psi_{S2^*}$	1.853e3/3.0E-5*	79E3*
H_2O adsorption on S2	$R_{3,f} = A_{3,f} \cdot x_{H_2O}^{1.7} \cdot \left(1 - \theta_{NH_3-S2^*} - \theta_{NH_4NO_3-S2^*} - \theta_{H_2O-S2^*}\right) \cdot \Psi_{S2^*}$	10.083	-
H_2O desorption on S2	$R_{3,b} = A_{3,b} \cdot \exp(-E_{3,b}/RT) \cdot \theta_{H_2O-S2^*} \cdot \Psi_{S2^*}$	10.083/9.4E-4	42E3*
NH_3 oxidation on S1	$R_4 = A_4 \cdot \exp(-E_4/RT) \cdot x_{O_2}^{0.5} \cdot \theta_{NH_3-S1^*} \cdot \Psi_{S1^*}$	8.61E3	75.7E3

NH_3 oxidation on S2	$R_5 = A_5 \cdot \exp(-E_5/RT) \cdot x_{O_2}^{0.5} \cdot \theta_{NH_3S2^*} \cdot \Psi_{S2^*}$	3.58E13	189E3
NO oxidation	$R_{6,f} = A_6 \cdot \exp(-E_6/RT) \cdot x_{NO} \cdot x_{O_2}^{0.5} \cdot \Psi_{S3^*}$	80E3	53E3
NO_2 decomposition	$R_{6,b} = A_6 \cdot \exp(-E_6/RT) \cdot x_{NO_2} \cdot \Psi_{S3^*} / K_{eq,NO-O_2}$	$K_{eq} = e^{-\Delta G/RT}$; ΔH : -58 kJ/mol; ΔS : -76.1 J/mol-K $\Delta G = \Delta H - T\Delta S$;	
Standard SCR on S1	$R_7 = A_7 \cdot \exp(-E_7/RT) \cdot x_{NO} \cdot \theta_{NH_3-S1^*} \cdot \Psi_{S1^*}$	6.3502E11	112.35E3
Standard SCR on S2	$R_8 = A_8 \cdot \exp(-E_8/RT) \cdot x_{NO} \cdot \theta_{NH_3-S2^*} \cdot \Psi_{S2^*}$	5.2164E9	78.545E3
NO_2 SCR on S1	$R_9 = A_9 \cdot \exp(-E_9/RT) \cdot x_{NO_2} \cdot \theta_{NH_3-S1^*} \cdot \Psi_{S1^*}$	7.7E14	144.6E3
NO_2 SCR on S2	$R_{10} = A_{10} \cdot \exp(-E_{10}/RT) \cdot x_{NO_2} \cdot \theta_{NH_3-S2^*} \cdot \Psi_{S2^*}$	6.6E13	130.14E3
NH_4NO_3 formation on S1	$R_{11} = A_{11} \cdot \exp(-E_{11}/RT) \cdot x_{NO_2} \cdot \theta_{NH_3-S1^*} \cdot \Psi_{S1^*}$	9.5E12	102.12E3
NH_4NO_3 reaction with NO on S1	$R_{12} = A_{12} \cdot \exp(-E_{12}/RT) \cdot x_{NO} \cdot \theta_{NH_4NO_3-S1^*} \cdot \Psi_{S1^*}$	2.5333E13	68.08E3
NH_4NO_3 formation on S2	$R_{13} = A_{13} \cdot \exp(-E_{13}/RT) \cdot x_{NO_2} \cdot \theta_{NH_3-S2^*} \cdot \Psi_{S2^*}$	9.5E12	102.12E3
NH_4NO_3 reaction with NO on S2	$R_{14} = A_{14} \cdot \exp(-E_{14}/RT) \cdot x_{NO} \cdot \theta_{NH_4NO_3-S2^*} \cdot \Psi_{S2^*}$	2.5333E13	68.08E3
NH_4NO_3 decompose on S1	$R_{15} = A_{15} \cdot \exp(-E_{15}/RT) \cdot \theta_{NH_4NO_3-S1^*} \cdot \Psi_{S1^*}$	3.04E13	96.61E3
NH_4NO_3 decompose on S2	$R_{16} = A_{16} \cdot \exp(-E_{16}/RT) \cdot \theta_{NH_4NO_3-S2^*} \cdot \Psi_{S2^*}$	3.04E13	96.61E3
N_2O formation with NO on S1	$R_{17} = A_{17} \cdot \exp(-E_{17}/RT) \cdot x_{NO} \cdot x_{O_2} \cdot \theta_{NH_3-S1^*} \cdot \Psi_{S1^*}$	3.44e12	110.0E3
N_2O formation with NO_2 on S2	$R_{18} = A_{18} \cdot \exp(-E_{18}/RT) \cdot x_{NO_2} \cdot \theta_{NH_3-S2^*} \cdot \Psi_{S2^*}$	9.72E13	129.9E3
N_2O oxidation	$R_{19} = A_{19} \cdot \exp(-E_{19}/RT) \cdot x_{N_2O} \cdot x_{O_2} \cdot \Psi_{S3^*}$	8.64E9	107.9E3

* The marked parameters are adapted from reference [45]; Ψ_{S1} = 50 mol/m^3; Ψ_{S2} = 50 mol/m^3; Ψ_{S3} = 50 mol/m^3. Ψ_{S1} are Ψ_{S2} represent the NH_3 storage sites; Ψ_{S3} represents the sites of NO oxidation and N_2O oxidation.

In addition, to properly account for the R11 and R12 reactions at NH_3 storage site S1, and R13 and R14 reactions at NH_3 storage site S2 in the stoichiometry of the fast SCR reaction, the model also considers the limitation of an equimolar NO/NO_2 reaction rate determined from the minimum mass flow between the NO and NO_2 gas species. Ψ_{S3} represents the density of sites for NO oxidation and N_2O oxidation. The SCR monolith geometry and material properties are assumed constant. The flow through the monolith channels is assumed to be laminar, hence the Nusselt number corresponding to laminar channel flow is used to compute the heat transfer rates. Table 3 lists the primary parameter values used in the model.

Table 3. The geometry, material properties, and catalyst loading parameters used in the NH_3-SCR model.

Parameters (unit)	**Value**
Void fraction ε (-)	0.8
Washcoat porosity ε' (-)	0.1
Channel density of the monolith (1/m^2)	620,000
Substrate density ρ_s (kg/m^3)	2500
Substrate conductivity k_s(w/m-K)	1.25
Substrate specific heat c_{ps} (J/kg-K)	840
Exhaust specific heat c_{ps} (J/kg-K)	1089
NH_3 storage capacity @S1 (mol/m^3) (i.e. Ψ_{S1})	50
NH_3 storage capacity @S2 (mol/m^3) (i.e. Ψ_{S2})	50
NO or N_2O oxidation activate site S3 (mol/m^3) (i.e. Ψ_{S3})	50

3. Experimental data

The tested Cu-SSZ-13 SCR catalyst is a commercial product used in diesel pickup trucks that was obtained from General Motors. The studied sample is a 2.0 cm diameter and 5.0 cm long core sample which was cut from a full-sized catalyst monolith with a molar Si/Al ratio of 15 and a molar Cu/Al ratio of 0.42. Prior to performing experiments, the core sample was degreened in a laboratory furnace at 800°C for 2 hours under a flow of 10% O2, 10% H2O and 80% N2. All of the experiments were conducted in an automated flow reactor at ORNL. The flow reactor uses synthetic exhaust gas mixtures to explore specific reaction functions and properties of catalytic materials. The catalyst core sample was loaded in a 2.5 cm diameter quartz tube with custom stainless steel end caps and placed in a tube furnace to control the catalyst temperature. Type K thermocouples were placed at the midpoint inside the core sample and 5 mm upstream and 5mm downstream to monitor and control the catalyst temperature. Gas concentrations upstream and downstream of the catalyst sample were measured with a MKS Multigas 2030HS Fourier Transform Infrared (FTIR) spectrometer.

A series of SCR reactor experimental procedures developed by ORNL [45] were used to explore the catalyst functions and measure exhaust properties used in the model (see Table S-1 in the supplementary document for the detailed protocol steps). For NH_3 oxidation, NO oxidation, and standard and fast SCR reactions testing at 175°C-550°C, the experimental procedures include 10 steps at each given temperature, including (1) a pretreatment/cooling process; (2) NH_3 adsorption; (3) NH_3 oxidation; (4) NH_3 inventory and NO oxidation; (5) NO SCR with NH_3/NO=1.0; (6) NO SCR with NH_3 inventory; (7) start NO_2; (8) NO+NO_2 SCR with NH_3/NOx=1.0 and NO/NOx=0.5; (9) NO+NO_2 SCR with NH3 inventory; and (10) a cleaning process. In the protocol steps, the pretreatment/cooling process takes 30minute to achieve a steady state at each given temperature, and the cleaning process is used to fully clean NH_3 inventory in the catalyst sample in order to ensure catalyst quality for testing at the next temperature condition. The space velocity (volumetric flow rate divided by the catalyst volume) of all tested cases is 60,000/hour.

To investigate the effects of NH_3 concentration and temperature on NH_3 storage capacity and stability of the catalyst, eight temperature programmed desorption (TPD) experiments were conducted. At each tested adsorption temperature, the experiment begins with 2-minutes of non-NH_3 flow, followed by an NH_3 adsorption step at 1000ppm; after the catalyst is saturated with NH_3, the NH_3 adsorption step is decreased in a stepwise manner to a NH_3 concentration of 800ppm, 600ppm, 400ppm, 200ppm, 100ppm, 50ppm, 25ppm, 12ppm and 0ppm; then the catalyst temperature is continuously increased to 800K at a rate of 5°C/min. All the inlet gas in the TPD experiments includes 5% CO_2 and 5% H_2O with a space velocity of 30,000/hour. To avoid significant NH_3 oxidation, the O_2 concentration is limited to 0.2% in these tests. Similar TPD experiments were used to investigate the effects of H_2O concentration and temperature on NH_3 storage capacity and stability, by repeating the measurements with the feed gas H_2O concentration decreasing from 10% 8.5%, 6.5%, 4.5%, 2.5% stepwise, with a 390ppm NH_3 inlet concentration and a space velocity of 30,000/hour.

4. Results

4.1. NH_3 and H_2O adsorption/desorption

Eight ammonia TPD experiments were used in validating the parameters over the range of adsorption temperature of 175°C -350°C. In each case, the experiment begins with 2-minutes of non-NH_3 flow, followed by an NH_3 adsorption step at 1000ppm; after the catalyst is saturated with NH_3, the NH_3 concentration is decreased stepwise; then the catalyst temperature is continuously increased to 800K at a rate of 5°C/min. All the inlet gas includes 5% CO_2, 5% H_2O and 0.2% O_2 with a space velocity of 30,000/hour. The results between the experiments and simulations at 175, 225, 275, 300 and 325°C are shown in Figure 1, and the results at 200, 250 and 350°C are provided in the supplementary document.

The observations show that the modeled ammonia storage and desorption matched very well to the measured NH_3 concentration. At the 1000ppm NH_3 inlet concentration, the outlet NH_3 concentration is initially zero, then increases and approaches 1000ppm for the cases with less than 300°C adsorption temperature; for the cases with 300°C adsorption temperature or above, the outlet NH_3 concentration is slightly less than 1000ppm. The main reason is that 0.2% O_2 leads to limited NH_3 oxidation at 300°C and beyond. When the inlet NH_3 concentration is reduced to 800ppm or lower in each step, a desorption of loosely bound ammonia is observed: the outlet NH_3 concentration remains higher than the inlet concentration for an extended period of time. This phenomenon becomes more significant at lower inlet NH_3 concentrations for the cases with adsorption temperature less than 300°C (see 400ppm or less inlet NH_3 concentration in Figure 1(a)-1(c)). During the NH_3 desorption phase near the end of each test, a NH_3 desorption peak is observed when the temperature is increased to 280-330°C. Another observation is that for temperatures of 300°C and higher only a very weak peak for NH_3 desorption is present (see Figure 1(d)-1(e)). The NH_3 storage capacity is reduced at higher temperature, and the loosely bound ammonia stored in low-temperature NH_3 storage sites (S2) are not effective at the higher temperature due to the higher energy of the NH_3 molecules. Thus,

the results indicate that the ammonia inventory in the SCR is bound differently at low and high temperature conditions, which supports the assumption of a two-site NH_3 storage mechanism with distinct low- and high-temperature storage characteristics.

In Figure 1(a) for 175°C, the simulated peak of desorption during TPD process has a slight shift to a higher transient temperature compared with the measurement. In the model, two fixed ammonia storage sites are considered for low and high temperature conditions, However, recent studies show that mobilized Cu ions can travel through zeolite and form transient ion pairs [47]. The dynamic and reversible formation of multinuclear sites from mobilized Cu ions can play a critical role in ammonia storage/desorption. Ignoring the reversible sites will limit the prediction accuracy across all temperature range. Thus, in future works, three or more ammonia storage sites should be considered to account for better SCR storage sites and actual ammonia storage.

Figure 2 shows the results of the simulated NH_3 storage site coverage during NH_3 adsorption and desorption TPD experiments at 175°C and 325°C using the model. Apparently, the coverage of the S1 high-temperature NH_3 storage sites remains fairly close to 1.0 without any significant impact from the inlet NH_3 variation during the 175°C case, except that the S1 coverage is reduced as the temperature increases continuously to 280°C after the NH_3 adsorption phase; on the other hand, the coverage of S2, representing the loosely bound, low-temperature NH_3 storage sites, varies substantially with different inlet NH_3 concentrations. Compared to the case of 175°C, the coverage of S1 at 325°C adsorption temperature becomes lower, and the adsorption coverage of S2 approaches zero except for inlet NH_3 concentrations more than 400ppm. This indicates that the SCR NH_3 storage capacity significantly depends on temperature and inlet NH_3 concentration, which was previously reported by Pihl et al. [45]. Consequently, the measured and simulated NH_3 storage capacity was compared as a function of adsorption temperature and inlet concentration. The results are shown in Figure 3(a). The data of the measured NH_3 storage capacity are derived from the eight ammonia TPD experiments shown in Figure 1. The data show that the SCR NH_3 storage capacity varies in equilibrium with both temperature and NH_3 concentration. The model based on the two-site storage mechanism does reflect this phenomenon and captures the SCR performance and mechanism very well.

The impact of water concentration on NH_3 storage capacity was also explored. The results plotted in Figure 3(b) detail NH_3 adsorption competing with H_2O as a function of temperature. The data of measured NH_3 storage capacity are derived from the eight H_2O TPD experiments, covering the range of adsorption temperature of 175-350°C. For these tests, the inlet gas included 390ppm NH_3 concentration, and the space velocity was 30,000/hour. The total composition is balanced by N_2 to achieve 100%. In each case, the experiment began with a flow of 2.5% H_2O for 1000s, and was then followed by a H_2O concentration step at 10%; after the catalyst is saturated with NH_3 at each operating condition, the NH_3 adsorption step is modified, in incremental steps, to evaluate H_2O concentration conditions of 10%, 9%, 7%, 5% and 3%. The results show that there is only about a 5% reduction in NH_3 storage capacity for the 11% H_2O case relative to the 3% H_2O case at 175°C, but at 325 °C, there is nearly no impact of H_2O concentration on the NH_3 storage capacity. Some examples showing the transient NH_3 data are plotted in Figure 4. Figure 4(a) clearly shows that at 1320s the NH_3 outlet concentration is increased dramatically when 3% H_2O is switched to 11% H_2O, meaning that significant adsorbed NH_3 is replaced by H_2O on the storage sites. Figure 4(a) also shows that the NH_3 outlet concentration drops slightly when the H_2O concentration is decreased to 9% or lower H_2O steps. This indicates some adsorbed H_2O is replaced by NH_3 on the storage sites. However, Figures 4(c) and (4d) show that the phenomenon becomes very weak at 250°C and even vanishes at 325°C. It shows that H_2O adsorption occurs only at the low-temperature storage sites, which is consistent with the model assumption that H_2O adsorption occurs at the low-temperature S2 storage sites. This can also be confirmed in Figure 2, as well as Figures 4(b), 4(d) and 4(e). Figures 4(b), 4(d) and 4(f) display the simulated storage coverage for NH_3 and H_2O during NH_3 adsorption competing with H_2O, for the cases shown in Figures 4(a), 4(c) and 4(e), respectively. Therefore, the H_2O competition with NH_3 during the adsorption process on Cu-SSZ-13 occurs mainly at low temperature, e.g. 175°C or less. In real diesel exhaust flows, H_2O adsorption may lead to weak SCR reaction efficiency, particularly during a cold-start.

Cite: Zhiming Gao, Josh Pihl, Tim LaClair, Brian Fricke. (2021) Global Kinetic Modeling of NH_3-SCR with Two Sites of NH_3 Storage on Cu-SSZ-13. Chemical Engineering Journal, Vol. 406, 127120. https://doi.org/10.1016/j.cej.2020.127120

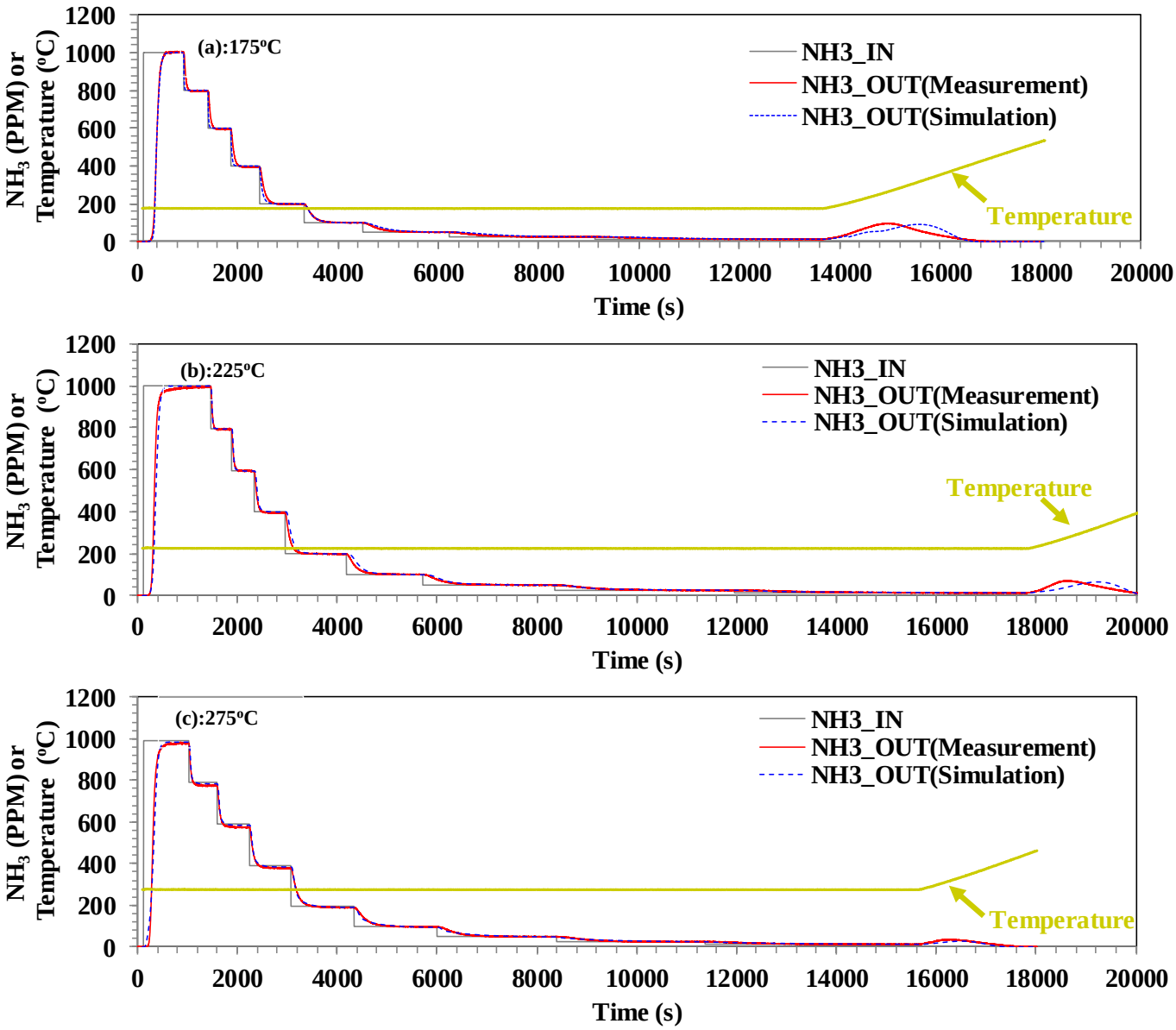

Cite: Zhiming Gao, Josh Pihl, Tim LaClair, Brian Fricke. (2021) Global Kinetic Modeling of NH_3-SCR with Two Sites of NH_3 Storage on Cu-SSZ-13. Chemical Engineering Journal, Vol. 406, 127120. https://doi.org/10.1016/j.cej.2020.127120

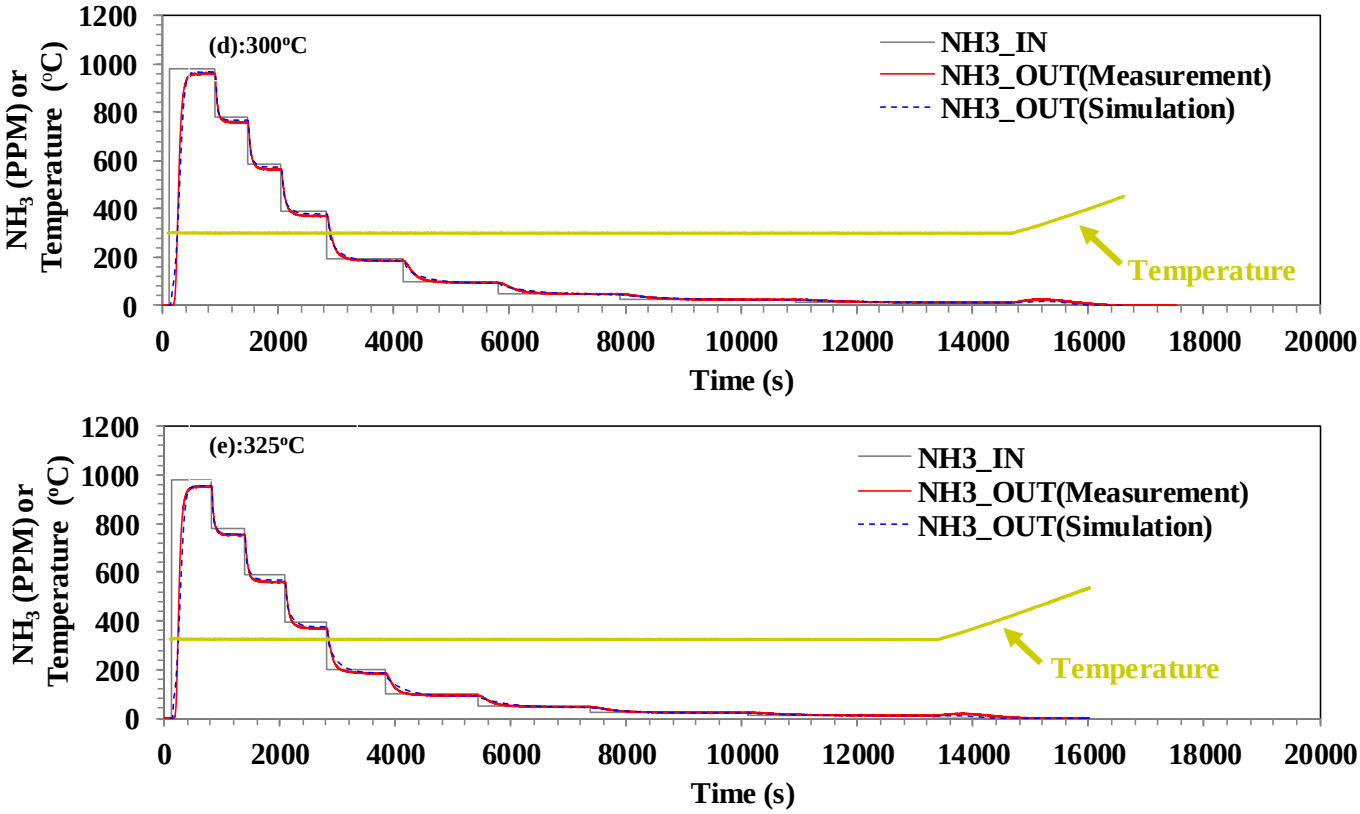

Figure 1: Measured and simulated NH_3 concentration during NH_3 adsorption and desorption TPD experiments; the NH_3 supply concentration was incrementally decreased with steps at 1000ppm 800ppm, 600ppm, 400ppm, 200ppm, 100ppm, 50ppm, 25ppm, 12ppm and 0ppm; after the 0 ppm step, the catalyst temperature was continuously increased to 800K at a rate of 5°C/min; the simulated emission gas supply to the catalyst also includes 5% CO_2, 5% H_2O and 0.2% O_2; the space velocity is 30,000/hour. The NH_3 adsorption temperatures at 175, 225, 275, 300 and 325°C for the plots shown in (a)-(e), respectively.

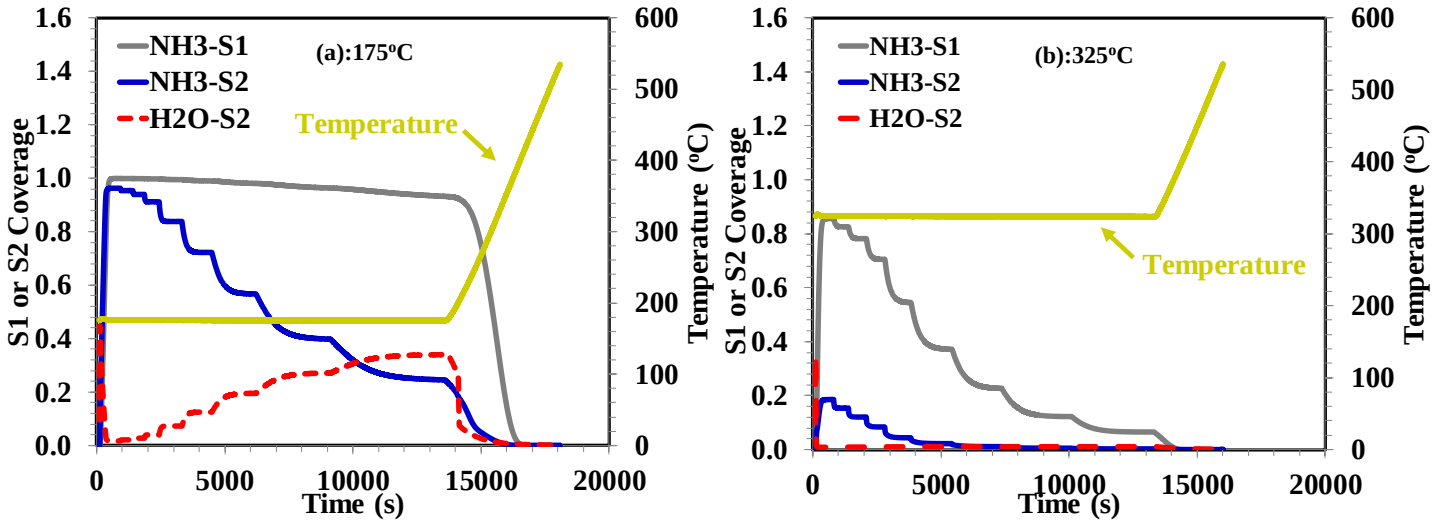

Figure 2: Examples of simulated NH_3 storage site coverage during NH_3 adsorption and desorption TPD experiments; the NH_3 adsorption temperatures are (a) 175°C and (b) 325°C.

Cite: Zhiming Gao, Josh Pihl, Tim LaClair, Brian Fricke. (2021) Global Kinetic Modeling of NH_3-SCR with Two Sites of NH_3 Storage on Cu-SSZ-13. Chemical Engineering Journal, Vol. 406, 127120. https://doi.org/10.1016/j.cej.2020.127120

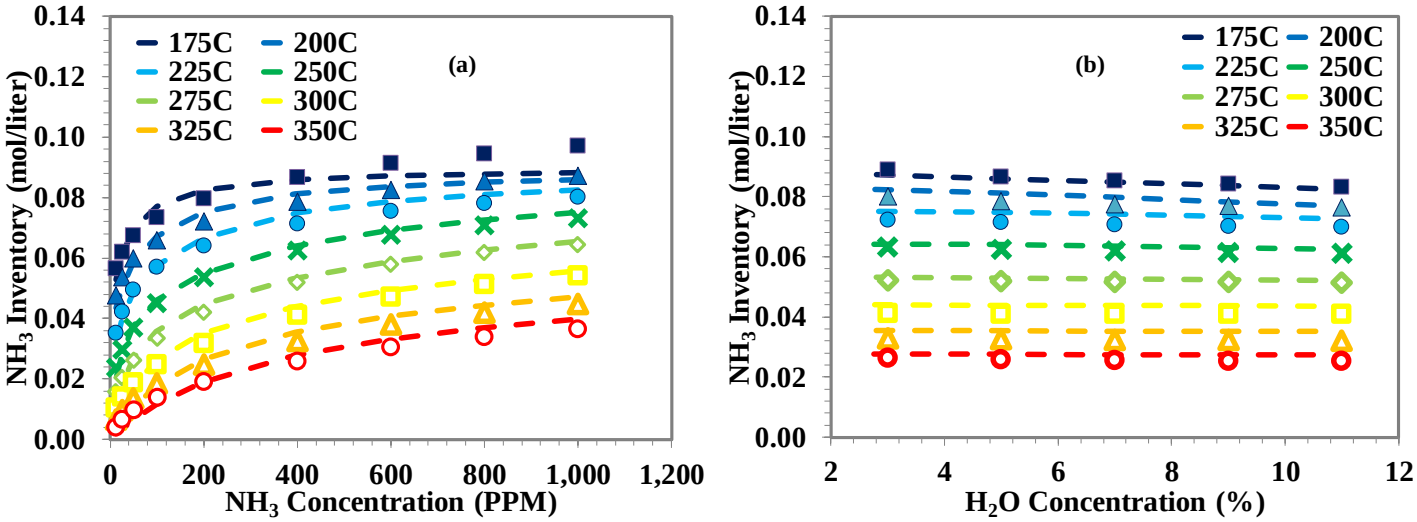

Figure 3: Comparison of measured and simulated NH_3 storage capacity as functions of (a) NH_3 inlet concentration and adsorption temperature, and of (b) H_2O concentration and adsorption temperature, to characterize the impact of water concentration and temperature on NH_3 storage.

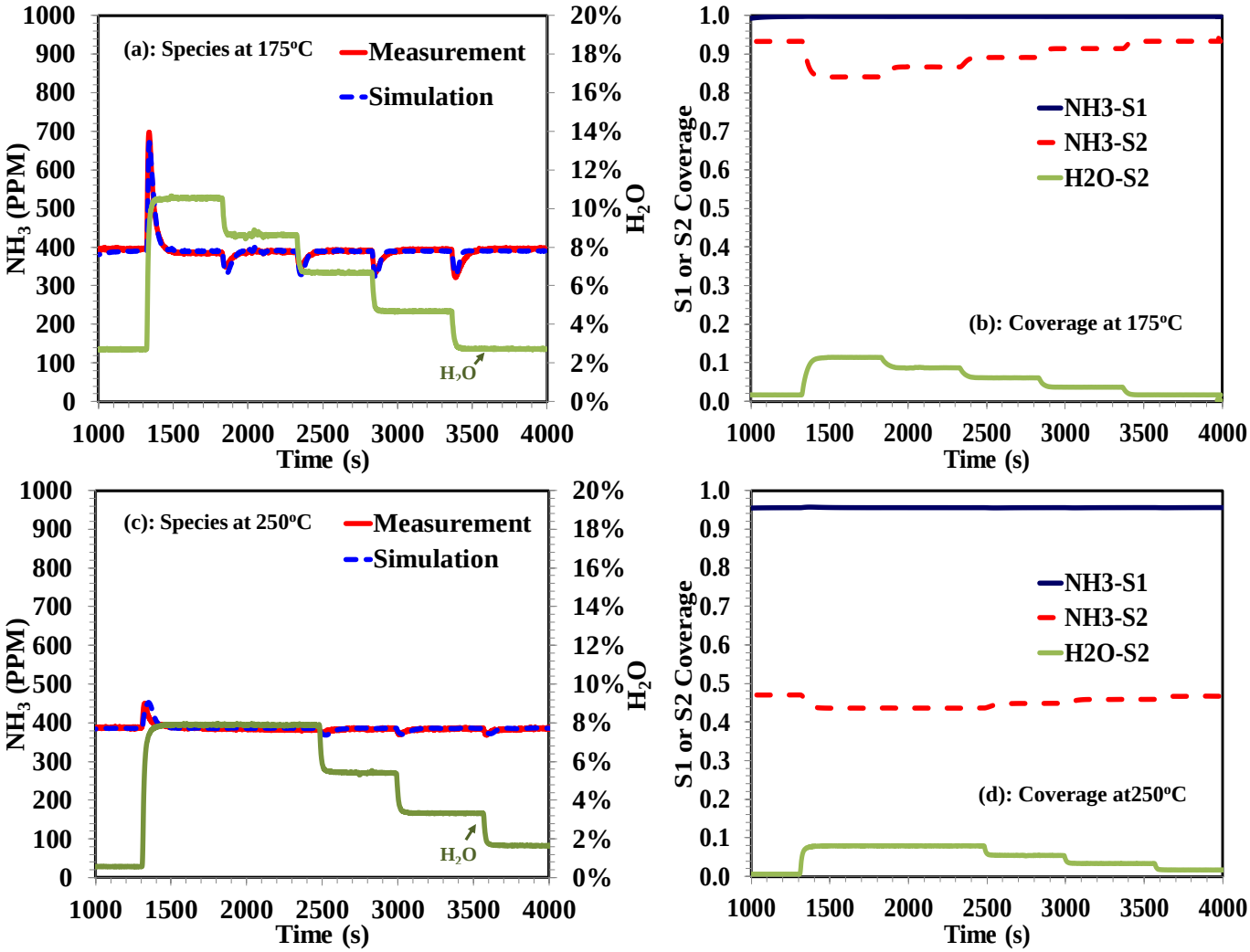

Cite: Zhiming Gao, Josh Pihl, Tim LaClair, Brian Fricke. (2021) Global Kinetic Modeling of NH_3-SCR with Two Sites of NH_3 Storage on Cu-SSZ-13. Chemical Engineering Journal, Vol. 406, 127120. https://doi.org/10.1016/j.cej.2020.127120

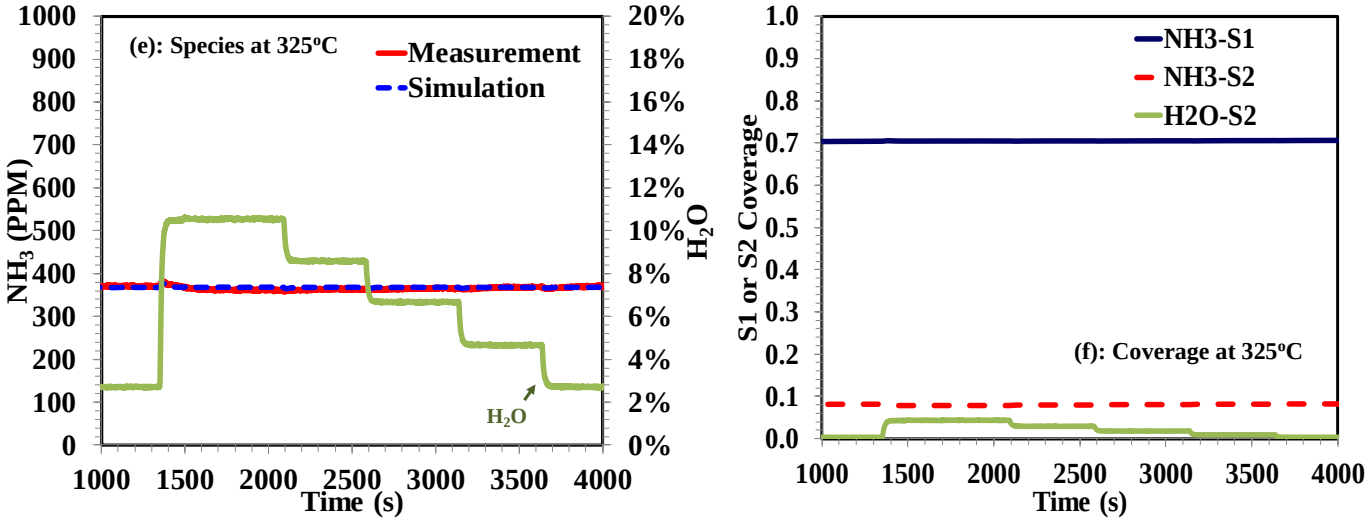

Figure 4: Measured and simulated NH_3 outlet concentration, as well as simulated storage coverages, during NH_3 adsorption completing with H_2O. The feed contains the decreased H_2O concentration of 11% 9%, 7%, 5%, 3% stepwise with 390 ppm NH_3 inlet concentration and a space velocity of 30,000/hour. The temperatures are 175, 250, and 325°C, respectively.

4.2. NH_3 oxidation and NO oxidation

Figure 5(a) and 5(b) compare the simulation with experimental results for NH_3 oxidation and NO oxidation, over a range of 250°C - 550°C and at the space velocity of 60,000/hour. In the NH_3 oxidation experiments shown in Figure 5(a), the catalyst was exposed to 300 ppm NH_3, 10% O_2, 5% H_2O, 5% CO_2 and a balance of N_2. Both the model and experiments show no ammonia oxidation taking place below 250°C. However, at 300°C and beyond, the ammonia oxidation increases significantly with the rise in temperature, as the proposed model predicts the measurement very well. This result of NH_3 oxidation can explain why the outlet NH_3 concentration in the case of 300°C adsorption temperature and higher is slightly less than the inlet NH_3 concentration, as shown in Figure 1. The adsorption cases contain 0.2% O_2 which could lead to limited NH_3 oxidation.

For the NO oxidation curve shown in Figure 5(b), the catalyst was exposed to 300 ppm NO, 10% O_2, 5% H_2O, 5% CO_2 and a balance of N_2. The current NO oxidation model predicts the basic features of the experimental NO oxidation very well. For example, at lower temperature, the NO oxidation conversion is kinetically limited and NO_2 production increases as the temperature increases. Thus, the NO_2 production reaches its peak around 450°C-500°C and then decreases due to thermodynamic constraints. In general, the model predicts the general trend of NH_3 and NO oxidations reasonably well.

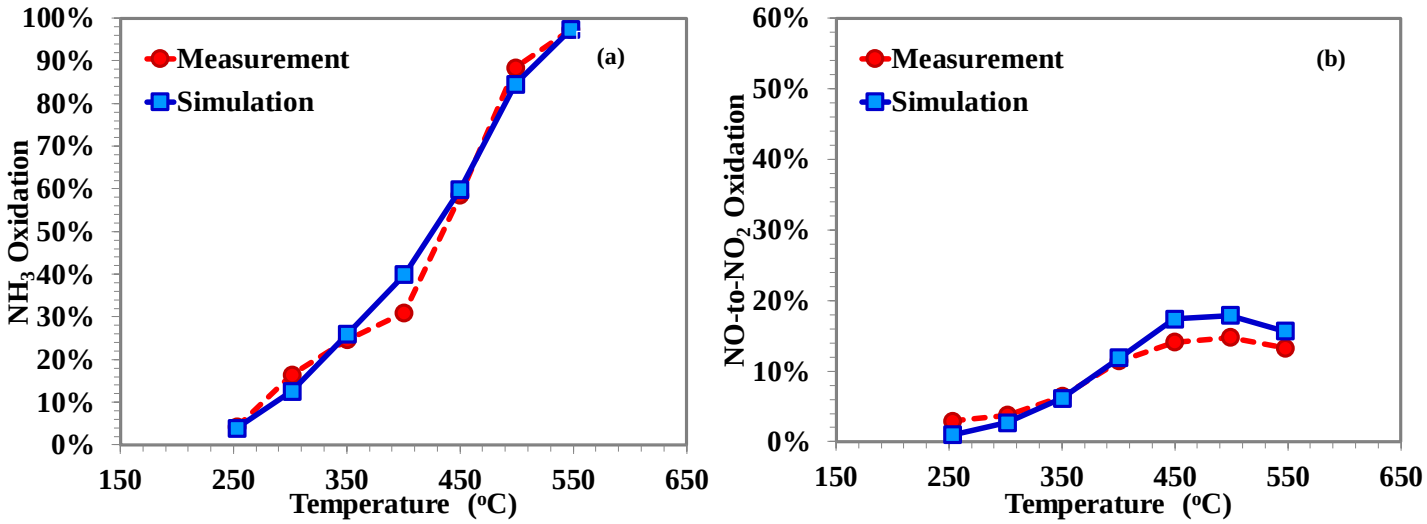

Figure 5: Simulated and experimental results for (a) NH_3 oxidation and (b) NO oxidation over the temperature range 250°C-550°C, at the space velocity of 60,000/hour.

4.3. NH_3 SCR

The experimental data measured from the ORNL SCR reactor experiment protocols were used for the SCR model development. For the standard SCR reactions, the catalyst was exposed to 300ppm NO, 300ppm NH_3, 5% CO_2, 5% H_2O and 10% O_2 over a temperature range of 150°C to 550°C with 25°C temperature increments. The space velocity was 60,000/hour. The comparison between the experimental data and predictions for the NO-SCR reaction is shown in Figure 6. The NOx reduction efficiency is fairly low at 150ºC, but increases dramatically between 150°C-200°C, enabling 90% or greater NOx reduction between 225°C-400°C; it then decreases with a further rise in temperature (see Figure 6(a)). The details for the outlet NO and NO_2 are shown in Figure 6(c) and 6(d), respectively. Figure 6(c) further shows more than 200ppm NO concentration at the outlet at 150°C, a reduction to near 20ppm at 250°C-400°C, and an increasing outlet NO concentration for 450°C -550°. A higher NO slip at 450°C-550°C is mainly due to significant NH_3 oxidation at that temperature (see Figure 5(a)), which leads to insufficient NH_3 available in the NO-SCR reaction. The predictions by the model capture the phenomenon reasonably well. Also the simulation error of NO is substantially less than the 15ppm error except below 200ºC. SCR reactions at low temperature are actually considerably different from those at high temperature, as SCR performance is degraded dramatically with even small temperature decline once below 200ºC. Although the current model does not fully resolve this, the results and general trends are still predicted with reasonable accuracy. Figure 6(d) shows limited NO_2 outlet concentration generated at 400°C or higher because of NO oxidation producing NO_2 (see Figure 5(b)). The simulation error of NO_2 is less than the 5ppm. Figure 6(e) compares the measured and predicted N_2O with no more than 10ppm error. The N_2O formation mechanism is fairly complicated, and extra-low N_2O levels are even more difficult in the modeling. Figure 6(b) and Figure 6(f) show comparisons of NH_3 reduction and outlet concentration, indicating a respectable accuracy of prediction. Similar to NO, the simulation error of NH_3 is substantially less than the 15ppm error except below 200ºC

In the fast SCR reactions, the catalyst was exposed to 150ppm NO, 150ppm NO_2, 300ppm NH_3, 5% CO_2, 5% H_2O and 10% O_2 over the temperature range from 150°C to 550°C, using 25°C temperature steps for all measurements. The space velocity remained at 60,000/hour. The results from the experiment and model predictions are compared in Figure 7. As expected, the NOx reduction in the fast-SCR reaction is higher than the standard SCR, particularly for the range of 150°C-200°C. Figure 7(c) and Figure 7(d) show a combined concentration of 200ppm for NO and NO_2 at the outlet at 150°C, and this decreases down to around 10-20ppm at 200°C-400ºC, and then increases over temperatures from 450°C-550°C. The main reason why fast SCR achieves the optimal performance at 200°C-400ºC is because this temperature range enables sufficient ammonia available for the SCR to react with the optimal equimolar NO to NO_2 rate, thus avoiding the degradation of SCR performance at lower temperature and avoiding the unbalance amount of NO, NO_2 and NH_3 reactants at higher temperature. The data actually shows a higher NO outlet concentration occurs at 450°C-550°C during the fast SCR reaction. This is caused by two mechanisms: (1) a thermodynamic constraint leads to NO_2 conversion to NO at 450°C; (2) significant NH_3 oxidation at that temperature, leading to insufficient NH_3 availability in the SCR reactions. Figure 7(e) displays the measured and predicted N_2O which, similar to the standard SCR reaction, also is not predicted as well as the NO and NO_2. However, the prediction level still reflects a reasonable level. Figure 7(b) and Figure 7(f) are the comparison of NH_3 reduction and outlet concentration, which is fairly good. Consequently, the model involved in R11-R14 reaction mechanisms is reasonably good at predicting the fast SCR performance. In Figure 7, the simulation errors of NO, NO_2 and NH_3 are substantially less than 15ppm except below 200ºC while the difference between the measured and predicted N_2O is less than 10ppm.

Figure 8 compares the measured and predicted SCR performance for the NO_2-SCR experiments as a function of temperature. In the slow SCR reactions, the catalyst was exposed to 225ppm NO_2, 300ppm NH_3, 5% CO_2, 5% H_2O and 10% O_2 while increasing the temperature from 225°C to 550°C in increments of 25°C. The NO_2-SCR reaction does not occur once below 200ºC. The results from the experiment and model predictions are plotted in Figure 8. In Figure 8(a), the NOx reduction in the slow-SCR reaction is substantially less than the standard SCR and fast SCR reactions (see Figure 6(a) and 7(a), respectively) for temperature less than 300°C. Although the model slightly over-estimates the NOx reduction in the range 450°C-550°C, the model does reasonably well overall in predicting the NO_2 SCR performance, as well as NO/NO_2/NH_3 concentration. In this case, the measured and predicted N_2O concentration matches reasonably well.

Cite: Zhiming Gao, Josh Pihl, Tim LaClair, Brian Fricke. (2021) Global Kinetic Modeling of NH_3-SCR with Two Sites of NH_3 Storage on Cu-SSZ-13. Chemical Engineering Journal, Vol. 406, 127120. https://doi.org/10.1016/j.cej.2020.127120

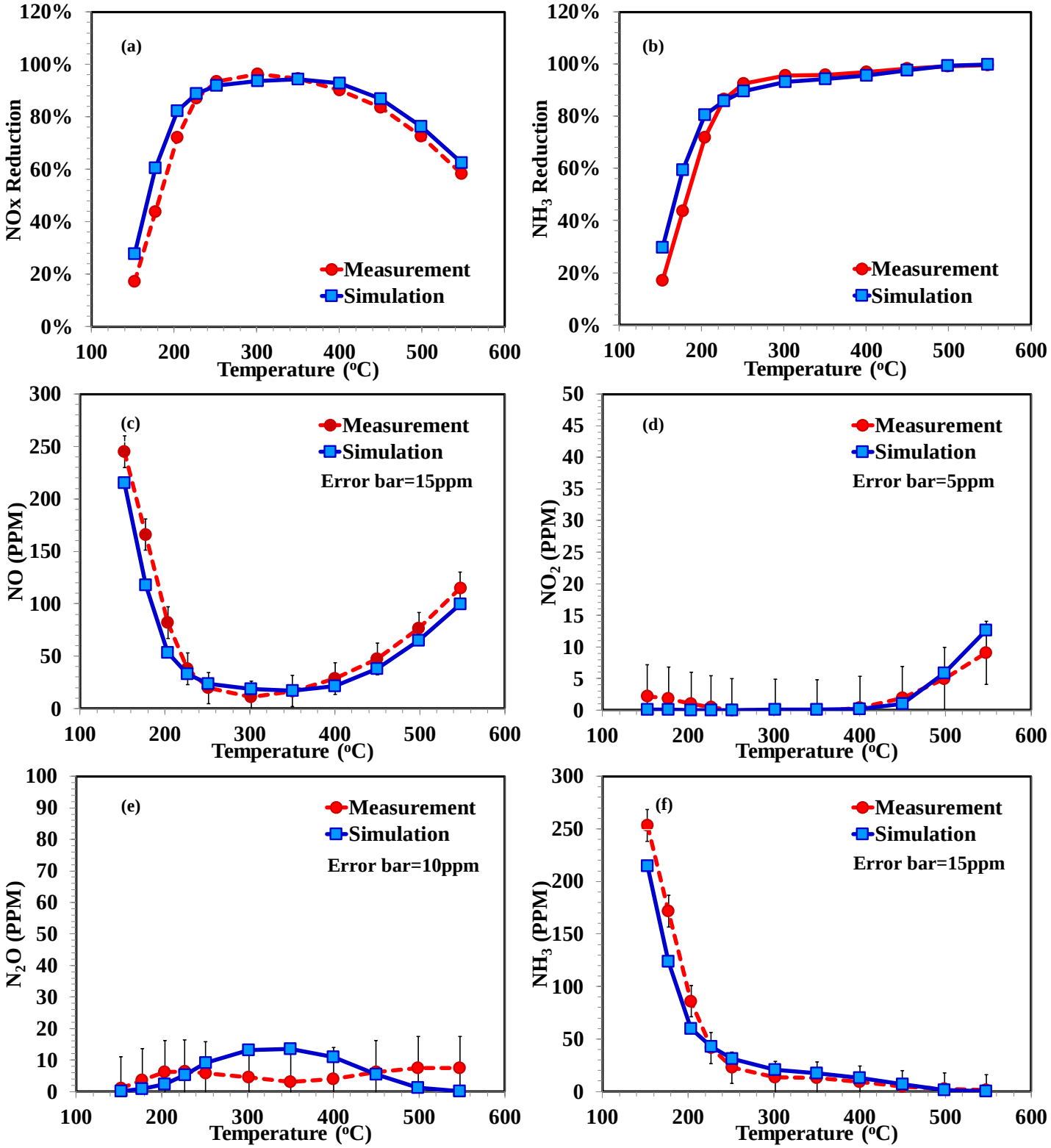

Figure 6: Measured and predicted SCR performance and $NO/NO_2/N_2O/NH_3$ outlet concentrations for the NO-SCR (standard SCR) reaction as a function of temperature, at a space velocity of 60,000/hour. The error bars for figures (c), (d), (e) and (f) are 15ppm, 5ppm, 10ppm and 15ppm, respectively.

Cite: Zhiming Gao, Josh Pihl, Tim LaClair, Brian Fricke. (2021) Global Kinetic Modeling of NH_3-SCR with Two Sites of NH_3 Storage on Cu-SSZ-13. Chemical Engineering Journal, Vol. 406, 127120. https://doi.org/10.1016/j.cej.2020.127120

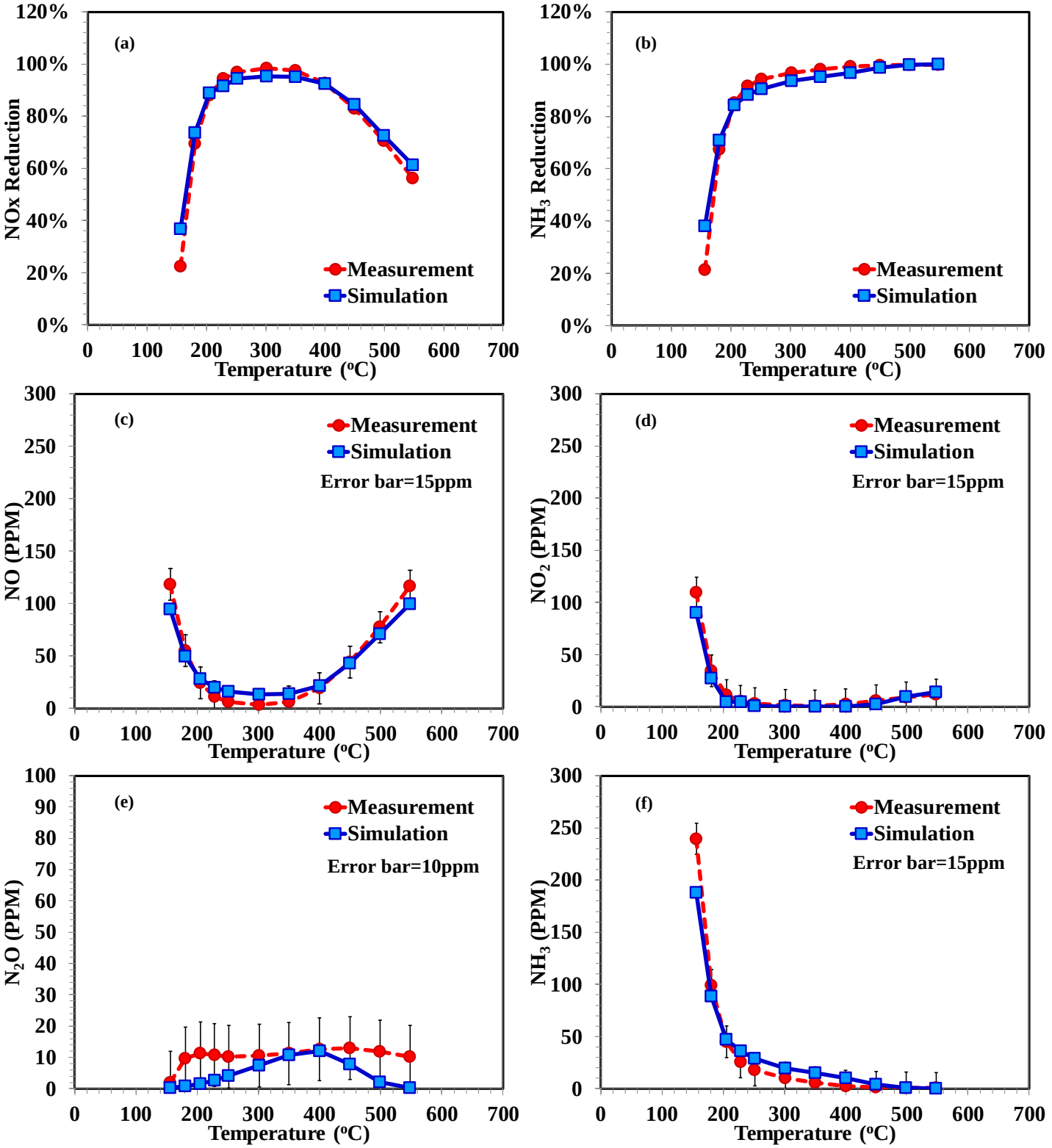

Figure 7: Measured and predicted SCR performance and $NO/NO_2/N_2O/NH_3$ outlet concentrations for the fast SCR reaction as a function of temperature, at a space velocity of 60,000/hour. The error bars at figures (c), (d), (e) and (f) are 15ppm, 15ppm, 10ppm and 15ppm, respectively.

Cite: Zhiming Gao, Josh Pihl, Tim LaClair, Brian Fricke. (2021) Global Kinetic Modeling of NH_3-SCR with Two Sites of NH_3 Storage on Cu-SSZ-13. Chemical Engineering Journal, Vol. 406, 127120. https://doi.org/10.1016/j.cej.2020.127120

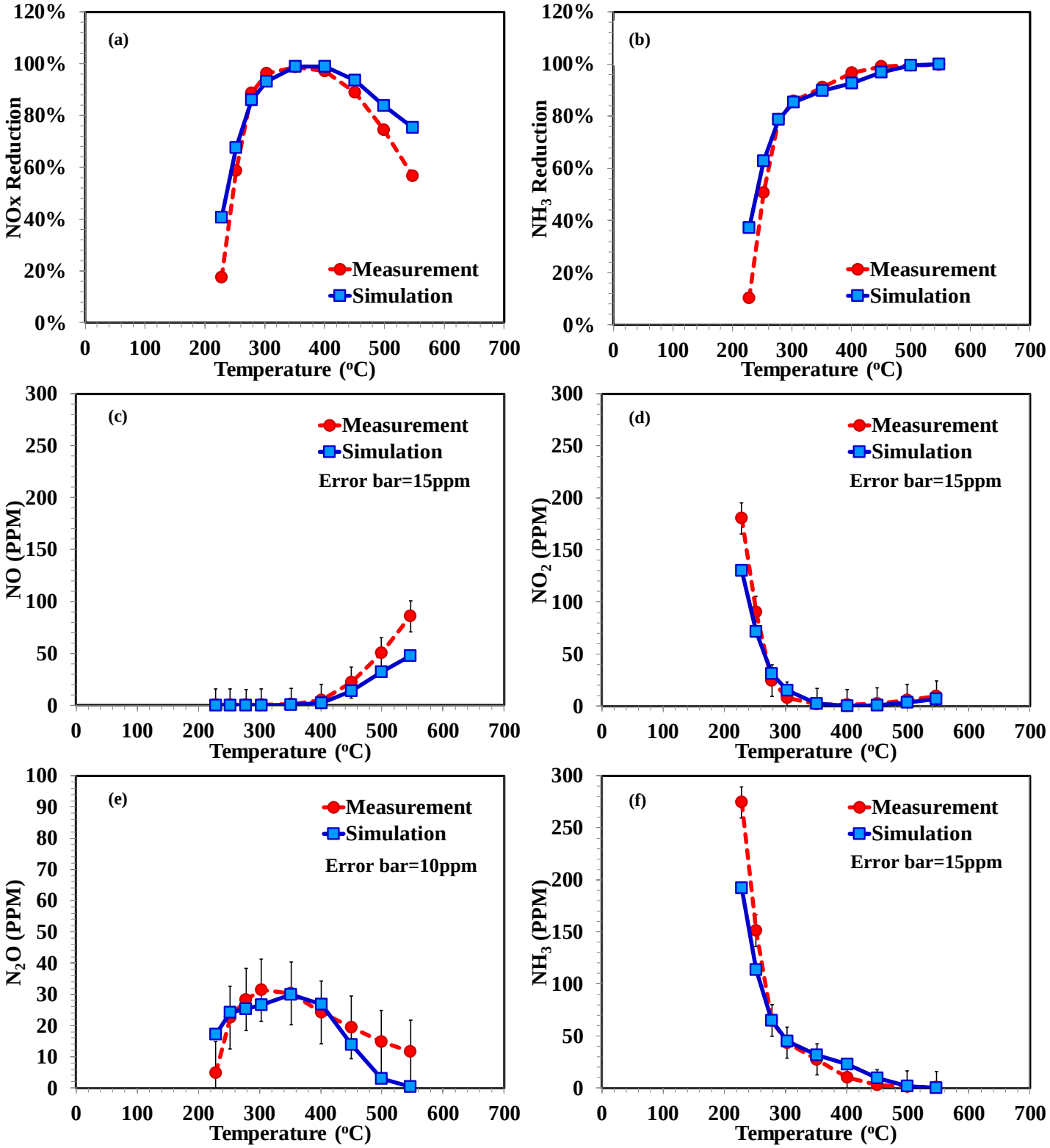

Figure 8: Measured and predicted SCR performance and $NO/NO_2/N_2O/NH_3$ outlet concentrations for the NO_2-SCR (slow SCR) reaction as a function of temperature, at a space velocity of 60,000/hour. The error bars for figures (c), (d), (e) and (f) are 15ppm, 15ppm, 10ppm and 15ppm, respectively.

4.4. SCR transient validation

The kinetic model developed was further validated with four additional transient experiments, which were not included in the model development and parameter fitting. The results cover 250°C -400 °C. Figure 9 shows the case tested at 250°C, and the other cases are attached in the supplementary document. Figure 9(a) details each step of $NO/NO_2/N_2O/NH_3$ inlet concentrations for a space velocity of 60,000/hour. Figure 9(b)-9(e) shows the resulting outlet concentrations for $N_2O/NO_2/NO/NH_3$. For the initial NH_3 adsorption step, only 300ppm NH_3 and 0.2% O_2 are added to the feed. The NH_3 is completely adsorbed at the beginning, but then the outlet NH_3 concentration gradually increases and finally reaches a steady-state level after about 800 seconds. The NH_3 oxidation step at 250°C does show a small change to the outlet concentrations due to NH_3 oxidation.

At the NH_3 inventory and NO oxidation step, Figure 9(b) shows a spike of overestimated N_2O at the beginning of NH_3 inventory while Figure 9(c) shows very limited NO_2 concentration due to NO oxidation. At the NO-SCR step, NO gradually decreases and approaches a steady-state level of ~20ppm. The model predicts very well the general trend of NH_3, NO and NO_2 —and even N_2O— concentrations as a result of implementing the two-site storage mechanism.

At the NO-SCR with NH_3 inventory step, the NO concentration is increased gradually and then maintains a value slightly less than 300ppm, while limited NO_2 is generated and N_2O disappears in absence of NH_3. The result of N_2O disappearance, together with a spike of N_2O at early NH_3 inventory, indicates that the formation of N_2O is related to the reaction of NH_3 and enriched NO, as is predicted accurately by the R17 mechanism of the model.

For the $NO+NO_2$ SCR step, without the supply of NH_3, the NO and NO_2 concentrations remain at 150ppm). Once NH_3 appears, both NO and NO_2 outlet concentrations gradually decrease and then reach a steady-state condition. Both the measurement and prediction show a small level of N_2O generated, although this is slightly underestimated by the model. At the $NO+NO_2$ SCR with NH_3 inventory step, the model reasonably predicts the NH_3 inventory consumption, outlet NO, NO_2 and N_2O concentration variation. The phenomena is predicted very well by the model reflecting the underlying mechanism.

The other three cases tested at 300°C, 350°C and 400°C, respectively, are shown in the supplementary document. These higher temperature cases have results very similar to those shown in Figure 9 shown for 250°C. The results confirm again that the model provides quite reasonable predictions of NH_3 consumption and outlet NO, NO_2 and N_2O concentration variations for the NO SCR, NO SCR with NH_3 inventory, start NO_2, $NO+NO_2$ SCR, and $NO+NO_2$ SCR with NH_3 inventory steps.

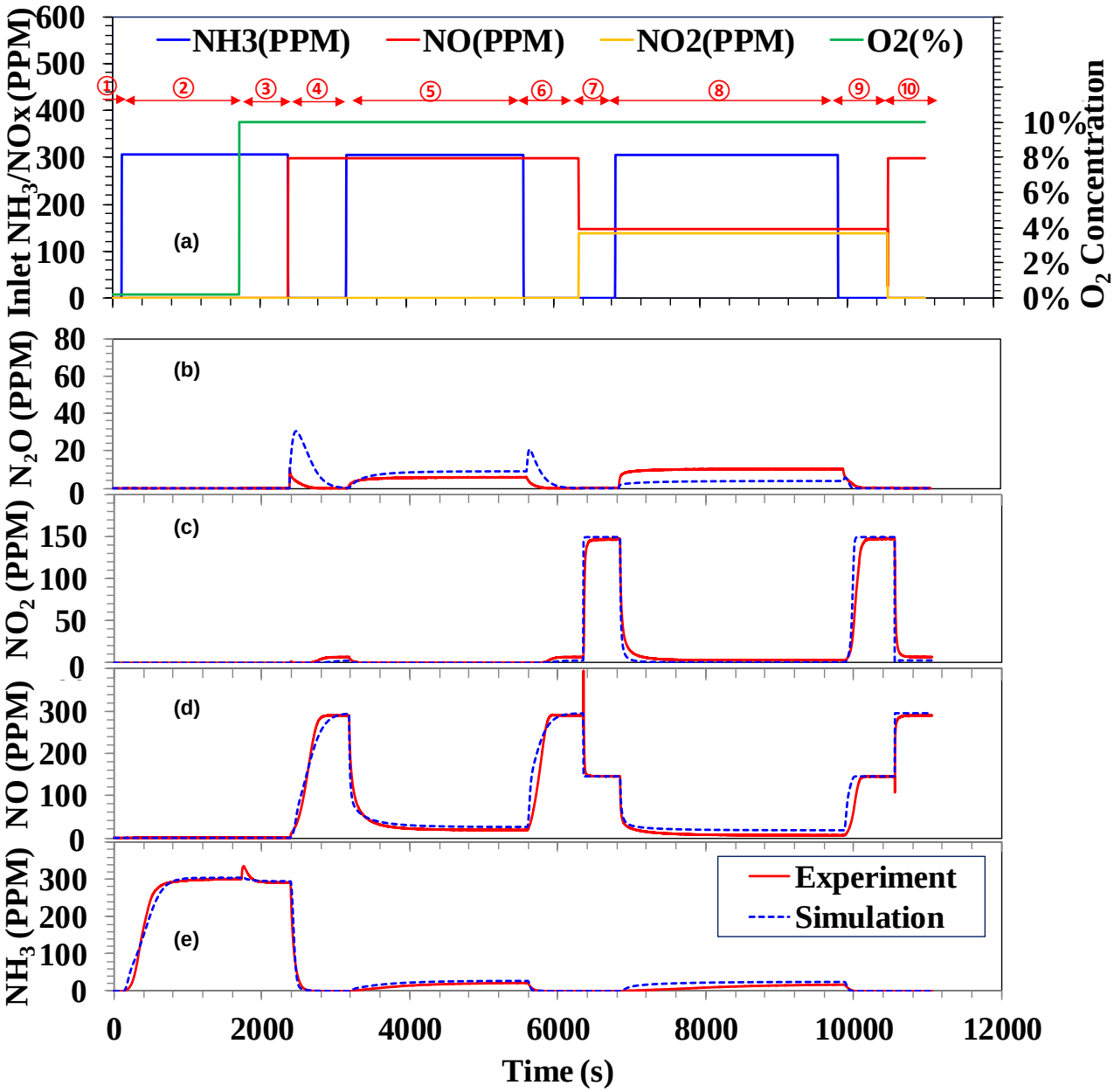

Figure 9: Measured and predicted transient SCR performance and NO/NO_2/N_2O/NH_3 concentrations at 250°C, for a space velocity of 60,000/hour. (1) Pretreat process; (2) NH_3 adsorption; (3) NH_3 oxidation; (4) NH_3 inventory and NO oxidation; (5) NO SCR with NH_3/NO=1.0; (6) NO SCR with NH_3 inventory; (7) start NO_2; (8) NO+NO_2 SCR with NH_3/NOx=1.0 and NO/NOx=0.5; (9) NO+NO_2 SCR with NH_3 inventory; (10) Cleaning process. (a) shows the inlet concentrations, while (b)-(e) show outlet concentrations for N_2O, NO_2, NO, and NH_3, respectively.

4.5. SCR model application in a light-duty vehicle driving cycle

The application of SCR models in vehicle simulations is valuable for aftertreatment design, development and optimization. Thus the developed SCR was integrated with an ORNL in-house DOC (diesel oxidation catalyst) model [25] via Matlab/Simulink, and the DOC/SCR model was further integrated with a conventional compact vehicle model developed using Autonomie [49], together with an ORNL transient engine model for lean exhaust emissions control. Autonomie is a powertrain and vehicle systems simulation platform. The transient engine model can estimate transient engine exhaust properties and fuel economy based on corrections to steady-state maps

[50, 51]. The conventional vehicle model is based on a 1701-kg, conventional, 2012 Ford Fusion powered by a 3.0-L, stoichiometric, gasoline engine and a 6-speed automatic transmission. The vehicle model has been validated over city and highway drive cycles, with prediction errors of +1.2%, +5.4% and -1.6% over the Urban Dynamometer Driving Schedule (UDDS), Highway Fuel Economy Test (HWFET) and Supplemental Federal Test Procedure (US06) cycles, respectively [52]. To investigate the impacts of DOC/SCR on lean exhaust emissions control, the stoichiometric gasoline engine in the simulated vehicle was replaced by a GM 1.9-L diesel engine. ORNL employed relevant engine maps for the diesel engine [52]; the DOC/SCR model consisting of a 1.2-L DOC and a following 2.6-L SCR catalyst was also implemented with the engine model for the modified vehicle model. In the drive cycle simulation, the SCR model does not account for vaporization and thermolytic conversion of the urea to ammonia. Instead, a simple urea injection strategy is assumed such that the instantaneous urea flow rate was adjusted to produce the optimal stoichiometric ratio of NH_3 to NO at the SCR catalyst inlet when the inlet temperature was above 150°C. For lower temperatures, urea injection was stopped.

Figure 10 shows the simulated DOC/SCR performance over a cold-start UDDS cycle beginning at 20ºC. Figure 10(a) shows the simulated temperature of the engine exhaust, DOC and SCR catalysts. The DOC and SCR temperatures correspond to the average solid temperature of the catalysts. As shown, the SCR catalyst temperature rise lags the engine-out exhaust and DOC catalyst temperature rise due to the device's thermal inertia. Thus it is clear that in addition to shifting SCR chemistry, the DOC can downgrade SCR performance by slowing the catalyst warm-up during a cold start. Figure 10(b) displays CO and HC cumulative emissions, as well as transient CO and HC oxidation during the first 150s. It is observed that nearly 100% of the CO and HC tailpipe emissions are contributed during the first 50s, i.e. the cold start. As shown in Figure 10(a), the DOC catalyst temperature is less than 200°C during the first 50s. The predicted CO and HC tailpipe emissions are summarized in Table 4, and both the CO and HC oxidation reduction is around 89%. The results for NOx emissions are plotted in Figure 10(c), showing a longer "light off" compared to CO and HC oxidation. The predicted NOx tailpipe emission is 0.0319g/km, and the SCR reduction efficiency is ~87%. By integrating with other catalyst models, the SCR model can provide unique insights for aftertretment design and optimization.

The SCR model was further used to explore the degrading impact of H_2O adsorption on the SCR performance. In the case, the H_2O adsorption competing with NH_3 is deactivated in the model. The result shows that the predicted NOx tailpipe emission is 0.0243g/km, and the SCR reduction efficiency is ~90%. The degrading potential of H_2O adsorption on SCR performance is ~24% on tailpipe NOx emissions reduction. Figure 10(d) compares the estimated impact of H_2O adsorption on cold-start NOx emissions during the first 100s of the UDDS beginning at 20ºC, and shows that H_2O adsorption leads to a worse SCR reaction efficiency during a cold-start. Thus, developing SCR technologies with anti-H_2O adsorption is considerably important to improve future SCR performance.

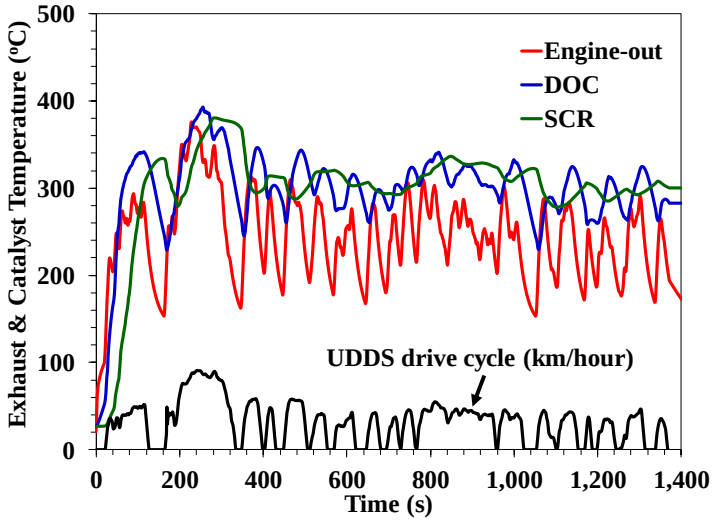

(a) Simulated temperature of engine exhaust, DOC and SCR catalysts

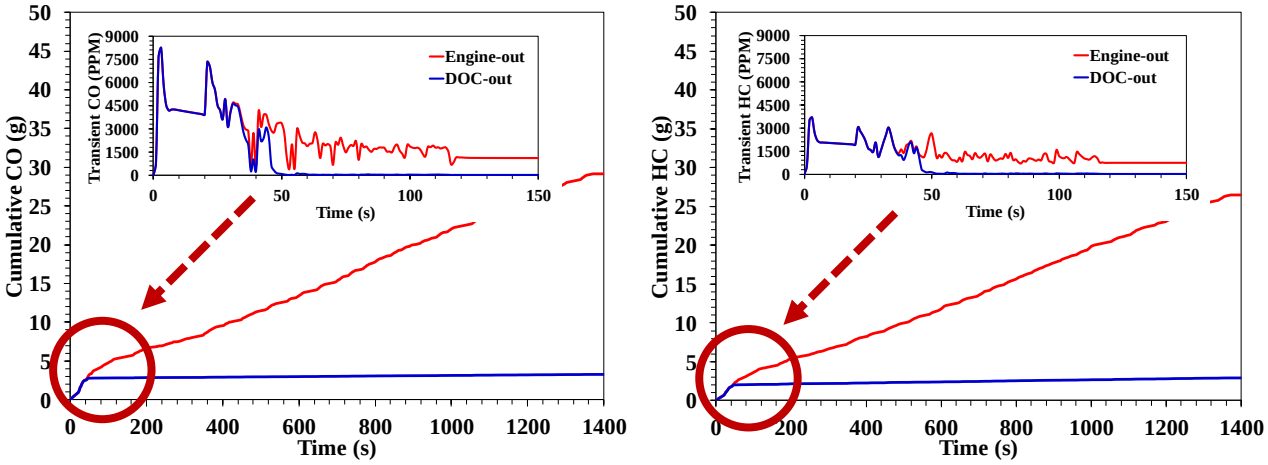

(b) CO and HC emissions

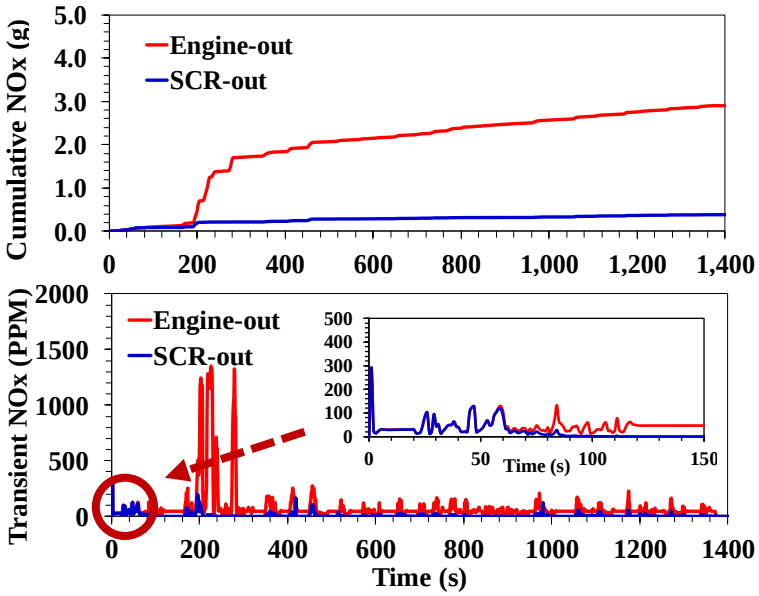

(c) NOx emissions

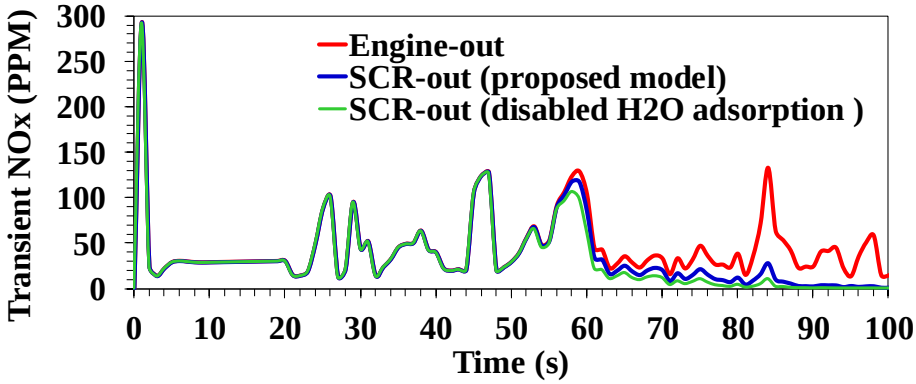

(d) Impact of H_2O adsorption on cold-start NOx emissions

Figure 10: Simulated performance of engine exhaust, DOC and SCR catalysts over a cold-start UDDS drive cycle beginning at 20°C; the simulated vehicle is a 1701-kg conventional vehicle powered by a GM 1.9-L diesel engine and a 6-speed automatic transmission.

Table 4. Summary of DOC/SCR emissions control

Emissions	CO	HC	NOx
Engine-out (g)	29.122	26.449	2.902

DOC/SCR-out (g)	**3.280**	**2.940**	**0.382**
DOC/SCR-out (g/km)	**0.274**	**0.245**	**0.032**
Reduction Efficiency	**88.7%**	**88.9%**	**86.8%**

5. Conclusion

A comprehensive two-site NH_3 storage SCR model is introduced to detail global kinetic reactions between the NH_3 and NOx reaching the SCR catalyst. The considered NH_3 inventory model includes two type of sites for NH_3 storage, as well as a H_2O storage mechanism at low temperature. SCR reactions are modeled at both sites, which have different high- and low-temperature characteristics for NH_3 adsorption/desorption. Moreover, the model includes the formation and decomposition of ammonium nitrate, and addresses N_2O relative to NO and NO_2 reactions with NH_3, as are observed from experiments. An in-depth understanding of such fundamental kinetic mechanisms is substantially important to evaluate SCR performance and exploit SCR catalyst materials. The model has been evaluated for commercial Cu-SSZ-13 measurements of NH_3 inventory, NH_3 oxidation, NO oxidation, standard SCR, fast SCR and NO_2 SCR. It provides reasonable steady-state prediction of NH_3 SCR performance and functions, and also predicts the transient SCR NH_3-NO-NO_2/O_2 reacting system with reasonable accuracy.

The proposed NH_3 inventory model based on two-sites of NH_3 storage captures the NH_3 storage behavior of a commercial Cu-SSZ-13 catalyst formulation very well over a wide range of adsorption temperatures. The simulated NH_3 site coverage at the two site types and their storage competing with H_2O provide an improved understanding of storage mechanisms as was observed in experimental data. For example, although the impact of competition between H_2O and NH_3 adsorption at the storage sites is very limited at steady-state high temperatures, the transient simulation shows that H_2O adsorption lead to a worse SCR reaction efficiency during a cold-start driving cycle. Developing SCR technologies with anti-H_2O adsorption is important to further improve SCR performance. Thus, the model can provide unique insights for the development of optimal SCR catalyst design and optimization.

The developed SCR model has been integrated with an ORNL in-house DOC model using Matlab/Simulink. The integrated model is capable of implementation into Autonomie and other commercial simulation software, and can be used to explore the impact of a DOC/SCR aftertreatment train system and model-based control strategies for optimal NH_3 dosing on lean exhaust emissions control. The SCR model can provide detailed emissions reduction estimation for transient drive cycles, understanding impact of cold starts, and can be integrated with other catalyst models for complex aftertreatment trains to explore innovative technologies for co-optimization of engine fuel economy and emissions control technologies.

Finally, all the experimental data and the code for the proposed model are attached in the supplementary documents, which can be used by potential readers.

Acknowledgments

This work was sponsored by the U.S. Department of Energy's ARPA-E and Vehicle Technologies office. The authors thank our Building Technologies Research and Integration Center (BTRIC) and National Transportation Research Center (NTRC) colleagues for their helpful discussion in this work. Additional thanks also go to the editors and reviewers for their support and volunteered time.

Nomenclature

A	Pre-exp factor, mole/mole-site-s
$c_{p,g}$	Specific heat of exhaust gas, J/kg-K
$c_{p,s}$	Specific heat of solid wall, J/kg-K
D_h	Characteristic diameter of SCR monolith channel, m
E_A	Activation energy, J/mol
G_a	External heat transfer surface per volume, 1/m
G_m	Surface area per volume of the monolith, 1/m

h_a	Convection heat transfer coefficient between ambient and catalyst exterior surface, W/m^2-K
h_g	Laminar-flow heat transfer coefficient, W/m^2-K
h_m	Laminar-flow mass transfer coefficient, m/s
k_s	Thermal conductivity of solid wall, W/m-K
K_{eq}	Equilibrium constant, -
$\dot{m}_g$	Exhaust gas mass flow rate, kg/s
Nu	Nusselt number, -
P	Pressure, Pa
Pr	Prandtl number, -
R	Gas constant, 8.314 J/mol-K
R^k	k-step chemical reaction rate, mol/m^3-s
Re	Reynolds number, dimensionless
S	Frontal surface area in the converter, m^2
Sc	Schmidt number, -
Sh	Sherwood Number, -
T_a	Ambient temperature, K
T_g	Exhaust gas temperature, K
T_s	Solid-wall temperature, K
t	Time, s
u_g	Exhaust gas velocity, m/s
ΔG	Gibbs free energy change at k-step reaction, J/mol
ΔH	Enthalpy change or reaction heat, J/mol
ΔS	Entropy change at the k-step reaction, J/mol-K
$x_{S,i}$	Mole fraction of ith species in solid phase, -
$x_{g,i}$	Mole fraction of ith species in gas phase, -
z	Flow moving direction, m

Greek symbols

ρ_g	Mass density of exhaust gas, kg/m^3
ρ_m	Mole density of exhaust gas, kg/m^3
ρ_s	Mass density of solid wall in the catalyst, kg/m^3
α_i^k	Stoichiometric coefficient of species *i* in *k*-step chemical reaction, -
ε	Hole space fraction of the monolith, -
ε'	Effective porosity of the channel wall surface, -

Superscripts

k	k-step reaction

Subscripts

a	Ambient
eq	Equilibrium
g	Exhaust gas
i	ith species
s	Solid substrate

Reference

1. Z. Gao, D.E. Smith, C.S. Daw, K.D. Edwards, B.C. Kaul, N. Domingo, et.al., The evaluation of developing vehicle technologies on the fuel economy of long-haul trucks, Energ. Convers. Manage., 106 (2015) 766-781.
2. R. Daya, C. Desai, B. Vernham, Development and validation of a two-site kinetic model for NH_3-SCR over Cu-SSZ-13. part 1. detailed global kinetics development based on mechanistic considerations, Emiss. Control Sci. Technol. 4(3) (2018) 143-171.
3. A.M. Beale, F. Gao, I. Lezcano-Gonzalez, C.H. Peden, J. Szanyi, Recent advances in automotive catalysis for NO x emission control by small-pore microporous materials, Chem. Soc. Rev. 44(20) (2015) 7371-7405.

4. W. Zhao, S. Dou, K. Zhang, L. Wu, Q. Wang, D. Shang, et.al., Promotion effect of S and N co-addition on the catalytic performance of V2O5/TiO2 for NH3-SCR of NOX, Chem. Eng. J. 364 (2019) 401-409.
5. H. Sjövall, E. Fridell, R.J. Blint, L. Olsson, Identification of adsorbed species on Cu-ZSM-5 under NH_3 SCR conditions, Top. Catal. 42(1-4) (2007) 113-117.
6. J.H. Park, H. J. Park, J.H. Baik, I.S. Nam, C.H. Shin, J.H. Lee, et.al., Hydrothermal stability of CuZSM5 catalyst in reducing NO by NH_3 for the urea selective catalytic reduction process, J. Catal. 240(1) (2006). 47-57.
7. S. Kieger, G. Delahay, B. Coq, B. Neveu, Selective catalytic reduction of nitric oxide by ammonia over Cu-FAU catalysts in oxygen-rich atmosphere, J. Catal. 183(2) (1999) 267-280.
8. S. Malmberg, M. Votsmeier, J. Gieshoff, N. Söger, L. Mußmann, A. Schuler, et.al, Dynamic phenomena of SCR-catalysts containing Fe-exchanged zeolites–experiments and computer simulations, Top. Catal. 42(1) (2007) 33-36.
9. D. Chatterjee, T. Burkhardt, M. Weibel, I. Nova, A. Grossale, E. Tronconi, Numerical simulation of zeolite- and V-based SCR catalytic converters, SAE Technical Paper 2007-01-1136, (2007).
10. M.P. Ruggeri, I. Nova, E. Tronconi, V. Schmeißer, M. Weibel, Modelling the hydrothermal ageing of a Fe-Zeolite catalyst for automotive NH3-SCR applications, Chemie Ingenieur Technik 90(6) (2018) 803-815.
11. K. Kamasamudram, N.W. Currier, X. Chen, A. Yezerets, Overview of the practically important behaviors of zeolite-based urea-SCR catalysts, using compact experimental protocol, Catal. Today 151(3-4) (2010) 212-222.
12. I. Nova, E.Tronconi, Urea-SCR technology for deNOx after treatment of diesel exhausts, Springer, New York, 2014, pp. 6-25.
13. D.W. Fickel, R.F. Lobo, Copper coordination in Cu-SSZ-13 and Cu-SSZ-16 investigated by variable-temperature XRD, J. Phys. Chem. C 114(3) (2009) 1633-1640.
14. S. Mohan, P. Dinesha, S. Kumar, NOx reduction behaviour in copper zeolite catalysts for ammonia SCR systems: a review, Chem. Eng. J. 384 (2020) 123253.
15. L. Ma, Y. Cheng, G. Cavataio, R.W. McCabe, L. Fu, J. Li, In situ DRIFTS and temperature-programmed technology study on NH_3-SCR of NOx over Cu-SSZ-13 and Cu-SAPO-34 catalysts, Appl. Catal. B: Environ. 156 (2014). 428-437.
16. K. Leistner, L. Olsson, Deactivation of Cu/SAPO-34 during low-temperature NH_3-SCR, App. Catal. B: Environ. 165 (2015) 192-199.
17. J.A. Dumesic, N.Y. Topsøe, H. Topsøe, Y. Chen, T. Slabiak, Kinetics of selective catalytic reduction of nitric oxide by ammonia over vanadia/titania, J. Catal. 163(2) (1996) 409-417.
18. B. Roduit, A. Wokaun, A. Baiker, Global kinetic modeling of reactions occurring during selective catalytic reduction of NO by NH_3 over vanadia/Titania-Based catalysts, Ind. Eng. Chem. Res. 37(12) (1998) 4577-4590.
19. J.C. Wurzenberger, R. Wanker, Multi-scale SCR modeling, 1D kinetic analysis and 3D system simulation, SAE Technical Paper 2005-01-0948, (2005).
20. H. Sjövall, R.J. Blint, A. Gopinath, L. Olsson, A kinetic model for the selective catalytic reduction of NOx with NH_3 over an Fe− zeolite catalyst, Ind. Eng. Chem. Res. 49(1) (2009). 39-52.
21. P.S. Metkar, M.P. Harold, V. Balakotaiah, Experimental and kinetic modeling study of NH_3-SCR of NOx on Fe-ZSM-5, Cu-chabazite and combined Fe-and Cu-zeolite monolithic catalysts, Chem. Eng. Sci. 87 (2013) 51-66.
22. H. Sjövall, R.J. Blint, L. Olsson, Detailed kinetic modeling of NH_3 SCR over Cu-ZSM-5, Appl. Catal. B: Environ. 92(1-2) (2009) 138-153.
23. S.A. Stevenson, J.C. Vartuli, C.F. Brooks, Kinetics of the selective catalytic reduction of NO over HZSM-5, J. Catal. 190(2) (2000) 228-239.
24. L. Olsson, H. Sjövall, R.J. Blint, A kinetic model for ammonia selective catalytic reduction over Cu-ZSM-5, Appl. Catal. B: Environ. 81(3-4) (2008) 203-217.
25. Z. Gao, C.S. Daw, V.K. Chakravarthy, Simulation of catalytic oxidation and selective catalytic NOx reduction in lean-exhaust hybrid vehicles, SAE Technical Paper 2012-01-1304, (2012). https://doi.org/10.4271/2012-01-1304 .
26. L. Olsson, K. Wijayanti, K. Leistner, A. Kumar, S.Y. Joshi, K. Kamasamudram, et.al., A multi-site kinetic model for NH_3-SCR over Cu/SSZ-13, Appl. Catal. B: Environ. 174 (2015) 212-224.
27. X. Song, G. Parker, J.H. Johnson, J. Naber, J. Pihl, A modeling study of SCR reaction kinetics from reactor experiments, SAE Technical Paper 2013-01-1576, (2013).
28. C.S. Daw, Z. Gao, D.E. Smith, T.J. LaClair, J.A. Pihl, K.D. Edwards, Simulated fuel economy and emissions performance during city and interstate driving for a heavy-duty hybrid truck, SAE Int. J. Commer. Veh. 6(1) (2013) 161-182.
29. X. Auvray, W. Partridge, J.S. Choi, J. Pihl, F. Coehlo, A. Yezerets, et.al., Kinetic modeling of NH 3-SCR over a supported Cu zeolite catalyst using axial species distribution measurements, Appl. Catal. B: Environ. 163 (2015) 393-403.
30. Y. Jangjou, C.S. Sampara, Y. Gu, D. Wang, A. Kumar, J. Li, W.S. Epling, Mechanism-based kinetic modeling of Cu-SSZ-13 sulfation and desulfation for NH 3-SCR applications, React. Chem. Eng. 4(6) (2019) 1038-1049.

31. N. Ghasemian, C. Falamaki, M. Kalbasi, Clinoptilolite zeolite as a potential catalyst for propane-SCR-NOx: performance investigation and kinetic analysis, Chem. Eng. J. 236 (2014) 464-470.
32. T. Selleri, I. Nova, E. Tronconi, An efficient reduced model of NH3-SCR converters for mobile aftertreatment systems, Chem. Eng. J. 377 (2019) 120053.
33. S. Shwan, J. Jansson, J. Korsgren, L. Olsson, M. Skoglundh, Kinetic modeling of H-BEA and Fe-BEA as NH_3-SCR catalysts—Effect of hydrothermal treatment, Catal. Today 197(1) (2012) 24-37.
34. G. Shibata, W. Eijima, R. Koiwai, K.I. Shimizu, Y. Nakasaka, Y. Kobashi, J. Kusaka, NH3-SCR by monolithic Cu-ZSM-5 and Cu-AFX catalysts: Kinetic modeling and engine bench tests, Catal. Today 332 (2019) 59-63.
35. S. Singh, D. Bhatia, Modeling the role of CO and C_3H_6 in NOx reduction on a Cu-CHA SCR catalyst, Chem. Eng. J. 377 (2019) 120311.
36. C. Ciardelli, I. Nova, E. Tronconi, D. Chatterjee, T. Burkhardt, M. Weibel, NH3 SCR of NOx for diesel exhausts aftertreatment: role of NO_2 in catalytic mechanism, unsteady kinetics and monolith converter modelling, Chem. Eng. Sci. 62(18-20) (2007) 5001-5006.
37. I. Nova, C. Ciardelli, E. Tronconi, D. Chatterjee, B. Bandl-Konrad, NH3–NO/NO_2 chemistry over V-based catalysts and its role in the mechanism of the fast SCR reaction, Catal. Today 114(1) (2006) 3-12.
38. Y.H. Yeom, J. Henao, M.J. Li, W.M. Sachtler, E. Weitz, The role of NO in the mechanism of NOx reduction with ammonia over a BaNa–Y catalyst, J, Catal. 231(1) (2005) 181-193.
39. M. Bendrich, A. Scheuer, R.E. Hayes, M. Votsmeier, Unified mechanistic model for standard SCR, fast SCR, and NO2 SCR over a copper chabazite catalyst, Appl. Catal. B: Environ. 222 (2018) 76-87.
40. J.A. Pihl, C.S. Daw, NH_3 storage isotherms: a path toward better models of NH_3 storage on zeolite SCR catalysts, DOE Crosscut Workshop on Lean Emissions Reduction Simulation, 2014.
41. Y. Tsukamoto, T. Fukuma, J. Kusaka, Analysis and modeling of NOx reduction based on the reactivity of Cu active sites and Brønsted acid sites in a Cu-chabazite SCR catalyst, SAE Technical Paper 2019-24-0150, (2019).
42. R. Daya, S.Y. Joshi, J. Luo, R.K. Dadi, N.W. Currier, A. Yezerets, On kinetic modeling of change in active sites upon hydrothermal aging of Cu-SSZ-13, Appl. Catal. B: Environ. 263 (2020) 118368.
43. P.S. Dhillon, M.P. Harold, D. Wang, A. Kumar, S.Y. Joshi, Modeling and analysis of transport and reaction in washcoated monoliths: Cu-SSZ-13 SCR and dual-layer Cu-SSZ-13+ Pt/Al2O3 ASC, React. Chem. Eng. 4(6) (2019) 1103-1115.
44. A. Srinivasan, S. Joshi, Y. Tang, D. Wang, N. Currier, A. Yezerets, Development of a kinetic model to evaluate water storage on commercial Cu-Zeolite SCR catalysts during cold start, SAE Technical Paper 2017-01-0968, (2017).
45. J. Phil, C.S. Daw, Energetics of NH_3 storage on zeolite SCR catalysts, DOE Crosscut Workshop on Lean Emissions Reduction Simulation, 2016.
46. Z. Gao, K. Chakravarthy, C. Daw, J. Conklin, Lean NOx trap modeling for vehicle systems simulations, SAE Int. J. Fuels Lubr. 3(1) (2010) 468-485.
47. Z. Gao, M.Y. Kim, J.S. Choi, C.S. Daw, J.E. Parks, D.E. Smith, Cold-start emissions control in hybrid vehicles equipped with a passive adsorber for hydrocarbons and nitrogen oxides, P.I. Mech. Eng. D-J. Aut. 226(10) (2012) 1396-1407.
48. Paolucci, I. Khurana, A.A. Parekh, S. Li, A.J. Shih, H. Li, et.al. Dynamic multinuclear sites formed by mobilized copper ions in NOx selective catalytic reduction. Science 357(6354) (2017) 898-903.
49. Autonomie. https://www.autonomie.net/, Accessed 2 July 2020.
50. Z. Gao, J.C. Conklin, C.S. Daw, V.K. Chakravarthy, A proposed methodology for estimating transient engine-out temperature and emissions from steady-state maps, Int. J. Engine Res. 11(2) (2010) 137-151.
51. Z. Gao, D. Deter, D. Smith, J. Pihl, C. Daw, I.I. Parks, Engine-aftertreatment in closed-loop modeling for heavy duty truck emissions control, SAE Technical Paper 2019-01-0986, (2019).
52. Z. Gao, S.J. Curran, J.E. Parks II, D.E. Smith, R.M. Wagner, C.S. Daw, et.al., Drive cycle simulation of high efficiency combustions on fuel economy and exhaust properties in light-duty vehicles, Appl. Energy 157 (2015) 762-776.